

High temperature equilibrium of 3D and 2D chalcogenide perovskites.

Prakriti Kayastha, Devendra Tiwari, Adam Holland, Oliver S. Hutter, Ken Durose, Lucy D. Whalley and Giulia Longo**

Prakriti Kayastha, Devendra Tiwari, Oliver S. Hutter, Lucy Whalley, Giulia Longo
Department of Mathematics, Physics and Electrical Engineering, Northumbria University,
Ellison Place, Newcastle upon Tyne NE1 8ST, United Kingdom

Devendra Tiwari
School of Chemistry, University of Bristol, Bristol BS8 1TS, United Kingdom

Adam Holland
HORIBA UK Limited, Kyoto Close, Moulton Park, Northampton NN3 6FL, United Kingdom

Ken Durose
Department of Physics, Stephenson Institute for Renewable Energy, Chadwick Building, Peach
St, Liverpool L23 9SD, United Kingdom

Keywords: Chalcogenide perovskites, Ruddlesden-Popper, BaZrS_3 , $\text{Ba}_4\text{Zr}_3\text{S}_{10}$, Raman spectroscopy, high temperature synthesis, thermodynamic equilibria

Abstract

Chalcogenide perovskites have been recently under the researchers' spotlight as novel absorber materials for photovoltaic applications. BaZrS_3 , the most investigated compound of this family, shows a high absorption coefficient, a bandgap of around 1.8 eV, and excellent environmental and thermal stability. In addition to the 3D perovskite BaZrS_3 , the Ba-Zr-S compositional space contains various 2-D Ruddlesden-Popper phases $\text{Ba}_{n+1}\text{Zr}_n\text{S}_{3n+1}$ (with $n = 1, 2, 3$) which have recently been reported. In this work it will be shown that at high temperature the Gibbs free energies of 3D and 2D perovskites are very close, suggesting that 2D phases can be easily formed at high temperatures. The analysis of the product of the BaS and ZrS_2 solid-state reaction, in different stoichiometric conditions, present a mixture of BaZrS_3 and $\text{Ba}_4\text{Zr}_3\text{S}_{10}$. To carefully resolve the composition, XRD, SEM and EDS analysis were complemented with Raman

spectroscopy. For this purpose, the phonon modes, and the consequent Raman spectra, were calculated for the 3D and 2D chalcogenide perovskites, as well as for the binary precursors. This thorough characterization demonstrates the thermodynamic limitations and experimental difficulties in forming phase-pure chalcogenide perovskites through solid state synthesis, and the importance of using multiple techniques to soundly resolve the composition of these chalcogenide materials.

Introduction

Chalcogenide perovskites (CPVK) have recently been proposed as possible non-toxic alternatives to lead-based perovskites for photovoltaic applications thanks to their promising optoelectronic characteristics, including a bandgap that is suited for tandem solar cell applications.^[1–4] Chalcogenide perovskites follow the formula ABX_3 with A, B and X representing an alkaline earth cation (2+), a transition metal cation (4+) and a chalcogenide anion (2-) respectively.^[5–7] The most studied compound in this family is $BaZrS_3$, but other compositions have been reported.^[8,9]

Accordingly, chalcogenide perovskites have been under recent scrutiny to evaluate and validate a variety of optoelectronic parameters. Reports suggest the possibility of tunable bandgaps through compositional engineering with high absorption coefficients in the visible range,^[10] low effective masses^[11] and, resultantly, high carrier mobilities.^[12] Moreover, these materials should present improved thermal and chemical stability compared with the hybrid halide perovskites, being resistant towards high temperatures and atmospheric conditions.^[13]

Notwithstanding these promising features, the development of CPVK-based devices is still hindered by the synthetic procedure necessary to prepare these perovskites. In practice, these materials need very high temperatures to be crystallized in the desired phase. For example, $BaZrS_3$ is produced by the solid-state reaction of the elemental or binary precursors at 800–1100°C for several hours or days. This requirement for high temperatures is limiting as it does not easily allow for thin film processing and device integration, and can lead to chalcogen loss via volatile precursors.

Understanding reaction mechanisms can help design fabrication procedures potentially having lower temperatures, and recent research has started to explore which processes may allow for this. For example, it has been proposed that favoring the formation of BaS_3 , which has a lower melting point than BaS , can trigger the formation of $BaZrS_3$ at temperatures as low as 600°C.^[14] Similarly,

it has been reported that an excess of sulphur in the reaction mixture can significantly reduce the reaction time and temperature.^[15]

The tuning of the precursors' stoichiometry can provide a path to find milder synthetic conditions for BaZrS_3 and other chalcogenide perovskites, but it can also lead to the formation of other unwanted perovskite phases. The ideal perovskite structure is formed from a three-dimensional network of corner sharing octahedra. However, there are other closely related perovskite-like phases that can be formed. For example, low dimensional Ruddlesden-Popper (RP) phases are known for chalcogenide perovskites, similarly to the oxide and halide perovskites. $\text{Ba}_{n+1}\text{Zr}_n\text{S}_{3n+1}$ for $n = 1, 2, 3$, (with the presence of low- and high-temperature polymorphs for $\text{Ba}_3\text{Zr}_2\text{S}_7$) have been reported in addition to the 3D structure BaZrS_3 (in which $n = \infty$).^[6,13,16–18] For the corresponding perovskites with Hf ($\text{Ba}_{n+1}\text{Hf}_n\text{S}_{3n+1}$), additional Ruddlesden Popper phases with $n = 4, 5$ have been reported,^[19] while no evidence is present for $n > 3$ in the Zr series. In these low dimensional phases, layers of 3D CPVK are alternated with layers of BaS , as represented in Figure 1. Interestingly, the bandgaps of these chalcogenide RP perovskites decrease as n increases, contrary to the oxide and halide counterparts, where the bandgap widens as n increases.^[20–22] The different crystalline structure not only affects the bandgap of the perovskite, but can also affect other functional features, such as carrier transport and thermal or chemical stability. A deep understanding of the synthetic reaction, especially when non-stoichiometric conditions are explored, will be essential to control the formation of competing phases with distinct properties. The most widely used technique for the assessment of different phases is X-ray diffraction (XRD). However, due to the structural similarity of the 3D and the 2D perovskites, the diffractogram peaks overlap, which make differentiating between species challenging. For example, in the case of samples formed by the mixture of BaZrS_3 and $\text{Ba}_3\text{Zr}_2\text{S}_7$, long data collection times and rigorous refinement (supported by compositional techniques such as Energy Dispersive X-ray Spectroscopy, EDS) are necessary to give a quantitative estimation of their compositions. As such, even with diffractograms presenting good angular resolution, intensity, and angular range, ambiguous assignation can still occur. It follows that good practice, especially for this family of materials, would be to combine crystallographic analysis with other complementary techniques that may also provide a clearer distinction between species. Vibrational spectroscopy is a good candidate technique to carry out this role, as it probes the local structure of a material, in contrast to XRD which probes the bulk response. In this letter it will be shown that the 3D and 2D

perovskite structures each have a unique vibrational fingerprint that better distinguishes between materials in the Ba-Zr-S system and that Raman spectroscopy is therefore well suited for checking the phase purity of the compounds.

In this study XRD and Raman spectroscopy are combined to assess the main composition of the product resulting from the solid-state reaction of BaS and ZrS₂ at various ratios. To aid in our analysis, a first-principles thermodynamic model is used to demonstrate that at high temperatures the Gibbs free energy of the 3D and 2D CPVK materials are only a few kJ/mol apart, indicating that both can be formed during high temperature synthesis (>1000K). In addition, the Raman spectra for all known binary and ternary compositions in the Ba-Zr-S phase systems are calculated from first-principles. Despite the use of excess ZrS₂ in the reaction mixtures, all the resulting powders show deficiency of Zr and S, and present mixtures of BaZrS₃ and the Ruddlesden-Popper phase Ba₄Zr₃S₁₀. It will also be shown that peaks' assignation can be done more confidently when Raman and XRD are used simultaneously. All calculated Raman spectra and the thermodynamic analysis code are published in open-access repositories alongside this work, allowing the adoption of our approach to other studies of BaZrS₃ synthesis.

Methods:

Experimental procedure:

Synthesis of powders: BaS (99.7%, Alfa Aesar) and ZrS₂ (99.99%, Alfa Chemistry) were used without further purification. 300 mg of powder formed by 1:1, 1:1.05, 1:1.1 and 1:1.2 molar mixtures of BaS and ZrS₂ (called Zr_0, Zr_5, Zr_10, Zr_20 respectively) were finely ground with an agate pestle and mortar, loaded into carbon-coated quartz ampules, purged with argon 3 times and sealed under a vacuum of 10⁻⁵ mbar. Each mixture was then placed in a single zone furnace at 500°C, and the temperature was increased to 900°C at a rate of 200°C/h. The powders were kept at 900°C for 5 days, and finally quenched in water.

Computational details:

Competing phases of BaZrS₃ were identified using the Materials Project database,^[23] with all Ba-Zr-S compounds within 0.5 eV above the convex hull considered. This energy range has been shown to cover the 90th percentile of all metastable materials reported within Materials Project.^[24,25] First principles density functional theory (DFT) calculations were carried out with

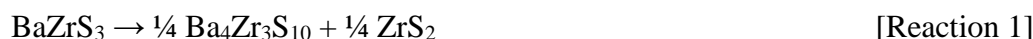
the all-electron numeric atom-centered code FHI-aims.^[26] Minimum-energy crystal structures were found using parametrically constrained geometry relaxation.^[27] The self-consistent field criteria was set to 10^{-7} e/Å³ and 10^{-6} eV/Å for electron density and force respectively. The structures were relaxed until the maximum force component was below 5×10^{-3} eV/Å. All other inputs were set to the default value within FHI-aims. All relaxations and phonon calculations were performed with the PBEsol^[28] functional with a tight basis set. Electronic band structures and total energies were calculated using the HSE06^[29] functional alongside inclusion of spin-orbit coupling. The resulting formation energies and band gaps are reported in Table S1. Phonon band structures were evaluated using the finite difference method with a 0.01 Å step size, as implemented in Phonopy.^[30] The supercell size and k-point spacing used for phonon calculations are presented in Table S2. Raman intensities and peak positions were generated through Phonopy-Spectroscopy with a two-point finite difference along displacements, and are reported in the Supporting Information.^[31] A Lorentzian peak width of 1 cm^{-1} was set on the peak positions obtained from the analysis. Macroscopic dielectric tensors were evaluated using the real space density functional perturbation theory method implemented in FHI-aims^[32] with the PBE functional.^[33] Gibbs free energies were calculated using Phonopy and the ThermoPot package.^[34] Imaginary modes were omitted from our calculation of the thermodynamic partition function and so do not contribute to the Gibbs free energy. An online repository containing i) analysis code for generating Figure 1a and Figure S2; ii) the raw data from electronic structure calculations; and iii) the data used to generate Raman spectra is available at https://github.com/NU-CEM/2022_BaZrS3_High-T_equilibrium.

Results and discussion

During BaZrS₃ synthesis competing phases can form from both the constituent elements (Ba, Zr, S) and/or from external impurities (e.g., O₂). In order to focus our analysis efforts on the thermodynamically accessible competing phases, ab-initio thermodynamic calculations were performed. As in this study synthesis was carried out within a closed ampule under vacuum, phases in the Ba-Zr-S system only were considered. Competing phases were initially identified using the Materials Project database,^[35] followed by re-calculation of the total energies using a higher level of theory (HSE06 functional with spin-orbit coupling) to reproduce lattice constants and bandgaps in agreement with published results from experimental studies: the formation energy, lattice

constants, electronic band gap and a comparison to experimental data for all systems considered are provided in the Table S1. Five competing ternary phases were identified: $\text{Ba}_4\text{Zr}_3\text{S}_{10}$ ($I4/mmm$), $\text{Ba}_3\text{Zr}_2\text{S}_7$ ($I4/mmm$), $\text{Ba}_3\text{Zr}_2\text{S}_7$ ($P42/mnm$), $\text{Ba}_3\text{Zr}_2\text{S}_7$ ($Cmmm$) and Ba_2ZrS_4 ($I4/mmm$). All ternary compounds are in the Ruddlesden Popper perovskite analogue series, $\text{Ba}_{n+1}\text{Zr}_n\text{S}_{3n+1}$.

It follows that there are three ternary-to-ternary decomposition mechanisms to consider:



To predict the relative phase stabilities a previously published methodology was followed to calculate the change in Gibbs free energy (ΔG) of each process,^[36,37] as this is the potential that is minimised in equilibrium. It is important to emphasize that this calculation does not consider the effects of lattice expansion or anharmonic vibrations. However, despite these limitations, this methodology has been used to successfully predict the temperature-pressure stability window for $\text{Cu}_2\text{ZnSnS}_4$.^[36]

The ΔG for all processes, reported in Figure 1a, is endothermic (positive valued) across the full temperature range considered (100K - 1300K). ΔG for [Reaction 3] ranges from 17kJ/mol to 15kJ/mol suggesting that BaZrS_3 is stable against decomposition into Ba_2ZrS_4 . ΔG for [Reaction 2] is calculated for the three polymorphs of $\text{Ba}_3\text{Zr}_2\text{S}_7$. At 300K ΔG is comparable for all three polymorphs, as expected given the structural similarity: 10kJ/mol ($P42/mnm$ and $Cmmm$), 11kJ/mol ($I4/mmm$). At 1300K ΔG is reduced to very small values: 7kJ/mol ($P42/mnm$), 6kJ/mol ($I4/mmm$) and 5kJ/mol ($Cmmm$). ΔG for [Reaction 1] is 10kJ/mol at RT reducing to 2kJ/mol at 1300K. Given that chemical accuracy is $\sim 4\text{kJ/mol}$, these results indicate that i) metastable $\text{Ba}_3\text{Zr}_2\text{S}_7$ and $\text{Ba}_4\text{Zr}_3\text{S}_{10}$ are energetically accessible during synthesis, with $\text{Ba}_4\text{Zr}_3\text{S}_{10}$ being the most likely phase to form ii) formation of $\text{Ba}_3\text{Zr}_2\text{S}_7$ and $\text{Ba}_4\text{Zr}_3\text{S}_{10}$ becomes more likely as the temperature is increased. Our results are supported by reports of $\text{Ba}_4\text{Zr}_3\text{S}_{10}$ formation during high-temperature synthesis of $\text{Ba}_3\text{Zr}_2\text{S}_7$.^[6]

Crystal, electronic and vibrational structure information for BaZrS_3 and for the lowest energy competing phase, $\text{Ba}_4\text{Zr}_3\text{S}_{10}$, are shown in Figure 1b-g. The electronic band structure is calculated with the HSE06 functional and includes spin-orbit effects, leading to an accurate predicted value

of 1.72 eV^[38] for the 3D perovskite direct band gap and a predicted value of 1.13 eV for the indirect band gap of the RP phase. This is the smallest predicted band gap for RP $\text{Ba}_{n+1}\text{Zr}_n\text{S}_{3n+1}$ materials considered, and is in line with previous reports of a decreasing band gap with increasing n .^[20-22] Whilst an indirect bandgap can lead to a decreased absorption coefficient near the band edge, we expect this to be counter-balanced by the flatter band dispersion for $\text{Ba}_4\text{Zr}_3\text{S}_{10}$, resulting in a larger density of states.

At room temperature BaZrS_3 is reported to form in in space group $Pnma$,^[9] which is a distortion of the idealised cubic perovskite. RP phases are reported to form in the space group $I4/mmm$.^[20-21] It is found that BaZrS_3 in the $Pnma$ phase is dynamically stable with positive phonon modes across the Brillouin zone. In contrast, $\text{Ba}_4\text{Zr}_3\text{S}_{10}$ is dynamically unstable with imaginary phonon modes at the zone boundaries. This indicates the presence of a symmetry lowering transition to a more stable phase at low-temperature, which is a common feature of halide and oxide perovskite materials.^[39,40] $\text{Ba}_4\text{Zr}_3\text{S}_{10}$ in the space group $Fmmm$ has also been previously reported in the literature.^[18] However this corresponds to a small lattice expansion and increase in the c/a lattice parameter ratio, so is unlikely to result from distortions along zone boundary phonon modes of the $I4/mmm$ phase. In Figures S1 we confirm that the high temperatures structures for $\text{Ba}_4\text{Zr}_3\text{S}_{10}$ ($Fmmm$), $\text{Ba}_3\text{Zr}_2\text{S}_7$ ($I4/mmm$) and Ba_2ZrS_4 ($I4/mmm$) also produce imaginary phonon modes in the harmonic approximation.

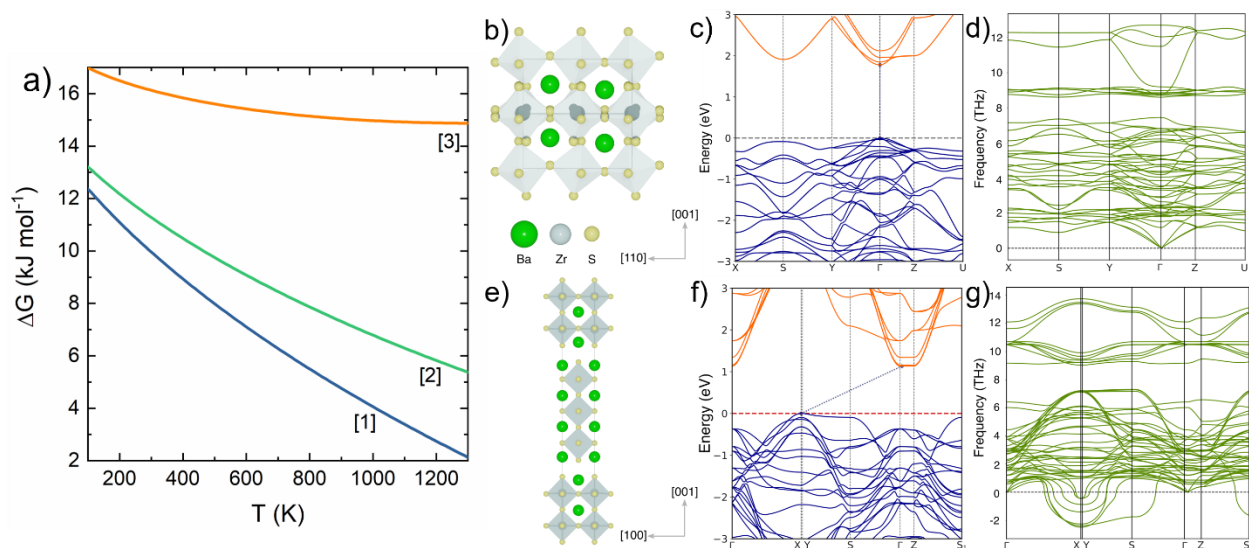


Figure 1: Thermodynamic, electronic and vibrational properties of BaZrS_3 ($Pnma$) and $\text{Ba}_{n+1}\text{Zr}_n\text{S}_{3n+1}$ ($I4/mmm$). a) Gibbs free energy ΔG as a function of Temperature. ΔG is calculated for decomposition of BaZrS_3 into: [1] $\text{Ba}_4\text{Zr}_3\text{S}_{10}$ and ZrS_2 ; [2] $\text{Ba}_3\text{Zr}_2\text{S}_7$ and ZrS_2 ; [3] Ba_2ZrS_4 and ZrS_2 . For comparison, all materials are in the $I4/mmm$ phase b) Crystal structure of BaZrS_3 c) Electronic band structure of BaZrS_3 calculated using the HSE06 exchange-correlation functional and with spin-orbit coupling (SOC), showing

a direct band gap of 1.72 eV^[38] d) Phonon band structure of BaZrS₃ with positive phonon modes across the Brillouin Zone, indicating dynamical stability. e) Crystal structure of Ba₄Zr₃S₁₀ f) Electronic band structure of Ba₄Zr₃S₁₀ (HSE06+SOC), showing an indirect band gap of 1.13 eV g) Phonon band structure of Ba₄Zr₃S₁₀ showing negative phonon modes at the zone boundaries, and indicating the presence of a lower symmetry structure at 0T.

To characterise the bulk structure, XRD was performed on powder samples at room temperature and ambient atmosphere. The corresponding diffractograms are reported in Figure 2a. The names Zr_0, Zr_5, Zr_10 and Zr_20 are used in this work represent the product obtained by the reaction of 1:1, 1:1.05, 1:1.1, 1:1.2 BaS:ZrS₂ molar ratios respectively.

Observing the diffractograms it can be noted that the samples present high crystallinity and, except the Zr_20, present complete conversion to the ternary phase, with no evidence of unreacted BaS (Figure S3a). The presence of unreacted ZrS₂ is more challenging to assess, as its characteristics peak is located at 32.2° (Figure S3a), where the samples present numerous small peaks which could derive also from the 2D or 3D perovskite. As discussed later in the text, Raman analysis simplified the assignation, confirming the presence of ZrS₂ in the Zr_0 sample. The Zr_20 sample presents an additional peak at low angles which origin has not been identified. Given the poor quality of the XRD pattern of this sample, both in terms of crystallinity and phase purity, it has been excluded from further characterization. It has to be noted that the presence of other Ba-S and Zr-S binary compositions have been excluded observing their XRD patterns and Raman spectra (Figure S3b). Similarly, the presence of oxides, sulfates and carbonates (all possible unwanted products in presence of air) have been excluded by comparing reported experimental XRD patterns and Raman spectra (Table S3).

The Zr_0 sample, which was expected to provide stoichiometric conversion to BaZrS₃,^[41] shows the presence of multiple phases that were assigned to the 3D BaZrS₃ and to the RP phase Ba₄Zr₃S₁₀. It is important to highlight the similarity of the angular position and intensity of the BaZrS₃, Ba₃Zr₂S₇ and Ba₄Zr₃S₁₀ XRD patterns, which complicates the experimental diffractograms resolution (Figure S4). The Rietveld refinement presented in Figure S5 and Table S4-6 shows that the RP phase is the majority one, representing almost the 70% by mass. As the molar amount of ZrS₂ in the starting mixture is increased by 5%, the diffractogram still reveals a mixture of phases, but with an overall predominance of the BaZrS₃ over the RP phase.

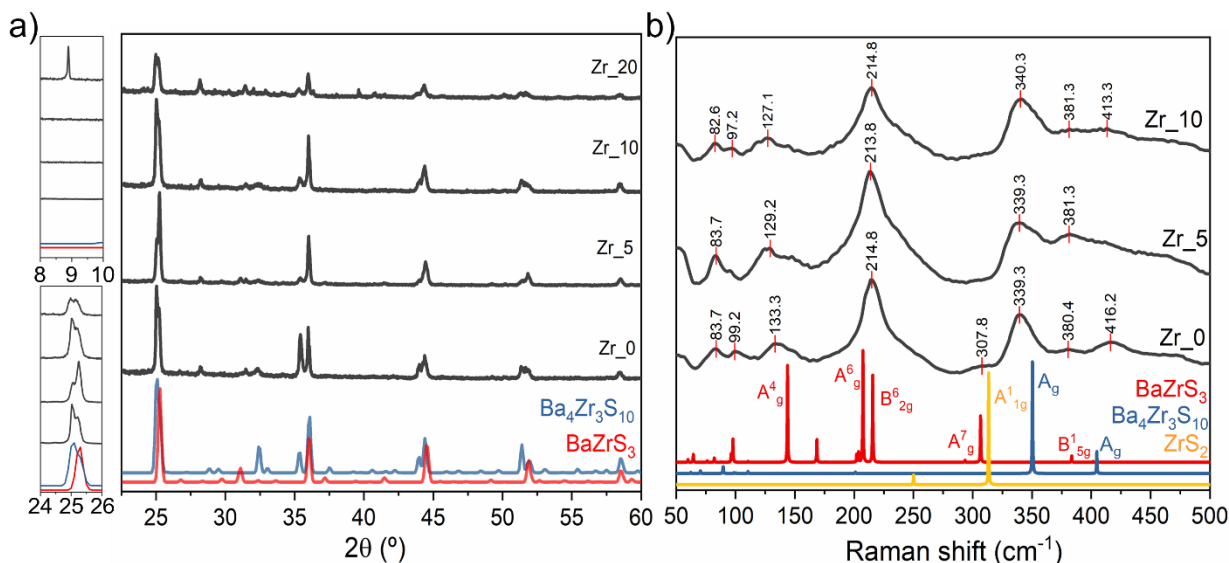


Figure 2 a) X-Ray diffractograms of the synthesized powders. Reference patterns for BaZrS_3 , $\text{Ba}_4\text{Zr}_3\text{S}_{10}$ are taken from ICSD (Collection Code 23288 and 72656 respectively). Top left panel: focus on the low angle peak shown by Zr_20. Bottom left panel: focus of the main peak. b) Calculated (bottom) and measured (top) Raman spectra collected with 785 nm excitation wavelength

This can be concluded by the change in shape of the peak at 25.1° and by observing the high angle peaks (Figure S4), and is confirmed by the Rietveld refinement. For the sample with a nominal 10% molar excess of ZrS_2 , $\text{Ba}_4\text{Zr}_3\text{Z}_{10}$ returns to be the majority phase, surprisingly reaching 86% of the sample weight.

Table 1. Phase quantification from Rietveld refinement

	BaZrS_3 (<i>Pnma</i>)	$\text{Ba}_4\text{Zr}_3\text{S}_{10}$ (<i>Fmmm</i>)	BaZrS_3 (<i>Pnma</i>)	$\text{Ba}_4\text{Zr}_3\text{S}_{10}$ (<i>Fmmm</i>)
	%wt	%wt	%mol	%mol
Zr_0	31	69	61	39
Zr_5	59	41	84	16
Zr_10	14	86	36	64

In Figure 2b and Table 2 the experimentally recorded Raman spectra of all the samples are reported together with the calculated spectra of BaZrS_3 , $\text{Ba}_4\text{Zr}_3\text{S}_{10}$ and ZrS_2 . First of all, it is worth stressing that the Raman spectra allows clear distinction between the binary sulphides, the 2D RP phases and 3D CPVK, in contrast with the XRD pattern in Figure 2a. At a first look it can already be appreciated that in all the samples there is BaZrS_3 , as shown by the most intense peak located at 214 cm^{-1} , deriving from the A_g^6 and B_{2g}^6 vibrational modes. Similarly, the peaks at lower angles

(83 and 133 cm^{-1}) and the peak at 380 cm^{-1} are mainly assigned to the BaZrS_3 phase (A_g^2 , A_g^4 and B_{1g}^5 respectively), in agreement with previous works (Table 2).^[5,40,41] It is worth stressing that the expected experimental spectra measured at room temperature should be red-shifted to lower frequencies compared to computational predictions, due to thermal expansion of the lattice which leads to a softening of the phonon modes. For the A_g^3 and A_g^4 modes in BaZrS_3 the frequency shift at room temperature is reported to be approximately 8 cm^{-1} ,^[42] in agreement with what observed (a shift of 10.3 cm^{-1} and 6.6 cm^{-1} respectively). In contrast, the experimental spectra are blue-shifted for the A_g^6 and B_{2g}^6 modes, as has been reported previously.^[42,44] Importantly, these modes relate to displacements of the sulphur species only. In the sample Zr_0 a shoulder can be observed around 308 cm^{-1} , which is assigned to both the A_g^7 mode of the BaZrS_3 as well as the A_{1g}^1 of the ZrS_2 . Since previously reported Raman spectra of BaZrS_3 show that the A_g^7 mode is visible only at low temperature,^[42] the 308 cm^{-1} peak in the Zr_0 spectrum is likely to derive from unreacted ZrS_2 . This demonstrates that the presence of ZrS_2 is easier to observe through Raman spectroscopy than through XRD.

Importantly, all the spectra present a peak at around 339 cm^{-1} which does not derive from the 3D perovskite. Comparing the measured spectrum with the calculated one for $\text{Ba}_4\text{Zr}_3\text{S}_{10}$ it is possible

Table 2. Raman peak positions for the measured Zr_0 (ν_{exp}) compared to the calculated value (ν_{pbisol}).

Material	Mode	ν_{pbisol}	ν_{exp}
BaZrS₃	A_g^3	94.0	83.7
	A_g^4	139.8	133.3
	A_g^6	204.9	214.8
	B_{2g}^6	213.1	214.8
	B_{1g}^5	389.1	380.4
ZrS₂	A_{1g}^1	313.4	307.8
Ba₄Zr₃S₁₀	A_g	350.1	339.3
	A_g	403.9	416.2

to assign it to the secondary RP phase, which is also corroborated by XRD. The Zr_0 sample presents an additional peak at 416 cm^{-1} , which can be assigned to the A_g mode of the $\text{Ba}_4\text{Zr}_3\text{S}_{10}$. This phonon mode involves displacement of the sulphur species only, as in the A_g^6 and B_{2g}^6 modes of the BaZrS_3 phase, which can be used to rationalise the unexpected blue shift to higher frequencies for the experimental spectra.

Importantly, Raman spectra cannot be used for quantitative analysis unless calibration with phase pure materials is performed. The higher intensity of the BaZrS_3 Raman peaks compared to the RP ones does not indicate a higher content in the sample, as demonstrated by the Rietveld quantifications. However, it is interesting to note how the ratio between the areas of the 339 cm^{-1} and 214 cm^{-1} peak decreases as 5% molar excess

of ZrS_2 is used in the starting mixture, suggesting that in this sample the orthorhombic 3-dimensional phase is favoured over the 2D. This hypothesis is supported by the disappearance of the peak at 99 cm^{-1} (which does not derive from BaZrS_3 and is attributed to the $\text{Ba}_4\text{Zr}_3\text{S}_{10}$ mode located at 92 cm^{-1}) and to the increased intensity of the 380 cm^{-1} peak. In the Zr_{10} sample, instead, the ratio between the two peaks returns in favour to the $\text{Ba}_4\text{Zr}_3\text{S}_{10}$, with a reduction of the BaZrS_3 peaks, as confirmed by Rietveld analysis. It should be noted that the measured Raman spectra were compared against the spectra of the binary precursors (Figure S3) as well as against the oxide counterparts (Table S3),^[45–49] confirming their absence in the synthesised mixture.

So far it has been shown that, in these synthetic conditions, the reaction between binary precursors leads to the formation of a secondary 2D ternary phase. Zr- or S-poor conditions can trigger the formation of RP phases, and a careful compositional analysis is necessary to obtain sensible conclusions. For this reason EDS compositional analysis has been performed on all the synthesized powders and on the Zr_0 precursor mixture before heat treatment, and the results are reported in Table 3.

Table 3: EDS quantifications (in atomic %) of the Zr_0 powder before the synthesis and after, Zr_5 and Zr_{10} with the instrumental error.

	Ba	Zr	S
Zr_0 before treatment	23 ± 5	22 ± 5	55 ± 5
Zr_0 after treatment	25 ± 5	21 ± 5	54 ± 5
Zr_5	25 ± 5	22 ± 5	53 ± 5
Zr_10	25 ± 5	23 ± 5	52 ± 5

The Zr_0 precursor mixture confirms that the Ba/Zr atomic ratio before heat treatment was 1:1. Surprisingly, all the resulting powders after treatment present Zr deficient compositions, with the Ba/Zr atomic ratio decreasing in the Zr_0 , Zr_5 and Zr_{10} series. However it is worth stressing that the confidence range of these values is enlarged by the limitations associated with powders analysis with EDS (see Supporting Information). The starting material and the synthesised powders also present sub-stoichiometric amounts of sulphur, which become more unbalanced as the starting excess of ZrS_2 is higher. To exclude accidental losses during the loading of the samples in the quartz ampules, a second batch repeating the Zr_0 conditions was prepared and characterized showing very similar XRD, Raman spectra and EDS compositions to Zr_0 (Figure S6). The systematic loss of Zr in these synthesis hints to possible unwanted reactions with the quartz ampule, even if carbon-coated. More investigation is needed to address this phenomenon, which

is out of the scope of this work. However this evidence hints that other precursors, rather than ZrS_2 , should be used, especially in high-temperature solid-state synthesis.

The observation of sub-stoichiometric amounts of Zr and S gives an additional explanation for the formation of $\text{Ba}_4\text{Zr}_3\text{S}_{10}$. As the RP $\text{Ba}_{n+1}\text{Zr}_n\text{S}_{3n+1}$ family of materials are a ZrS_2 -deficient analogue of BaZrS_3 , the RP phases are expected to be more readily formed in Zr- or S-poor environments. To explore this further, a ternary phase diagram for the Ba-Zr-S system was constructed using the first-principles thermodynamic model introduced earlier (Figure S2). This allows a prediction of which products are formed for the sub-stoichiometric amounts of Zr and S as measured by EDS. At high temperature all RP phases and most binary phases (all except BaS_3) lie on the convex hull, so that the predicted products are very sensitive to composition. Using Ba-Zr-S composition values within the range of values reported for each sample in Table 3, the model predicts that $\text{Ba}_4\text{Zr}_3\text{S}_{10}$ and BaZrS_3 will be formed at at 900°C , alongside a smaller proportion of ZrS_2 (Table S7). This suggests that there is an additional driving force for phase separation into BaZrS_3 and $\text{Ba}_4\text{Zr}_3\text{S}_{10}$ resulting from the under stoichiometric amount of Zr and S. Our modelling also suggests that the S concentration in the samples limits the formation of BaZrS_3 . This is why the Zr_10 sample, with the lowest proportion of sulphur measured by EDS, produces the highest proportion of $\text{Ba}_4\text{Zr}_3\text{S}_{10}$. On the other hand, this sample has the Ba/Zr ratio closer to unity, suggesting that the cation ratio is not the driving force for the preferential formation of 3D over 2D perovskites.

The compositional mapping presented in Figure 3 offers an additional insight in the nature of the synthesised powders. In the image, brighter zones correspond to areas of high atomic concentration, although it is recognised that shadowing effects give large dark areas (observable in the dark large areas in the mappings but not in the secondary electron images). Notwithstanding this, it may be observed that in all the samples Zr is less uniformly distributed than Ba and S, as evidenced by the particularly bright area in the Zr mapping. Among all the samples, the Zr_0 shows the biggest agglomeration of zirconium. Brighter area can be observed also in the other samples, but the dimension and number of these agglomerates reduces in Zr_5 and Zr_10 with the formation of smaller clusters more dispersed across the sample. The EDS analysis confirmed the presence of Zr-rich clusters in the sample Zr_0 (Figure S7), but in the others the distribution of Zr looks more homogeneous (Figure S8 and S9), even if some local deviations from the average are still present, as indicated by the mapping results. Instead, Ba and S mapping show that the Zr-rich areas in the Zr_0 sample correspond to S and Ba deficient zones. The presence of Zr-rich clusters

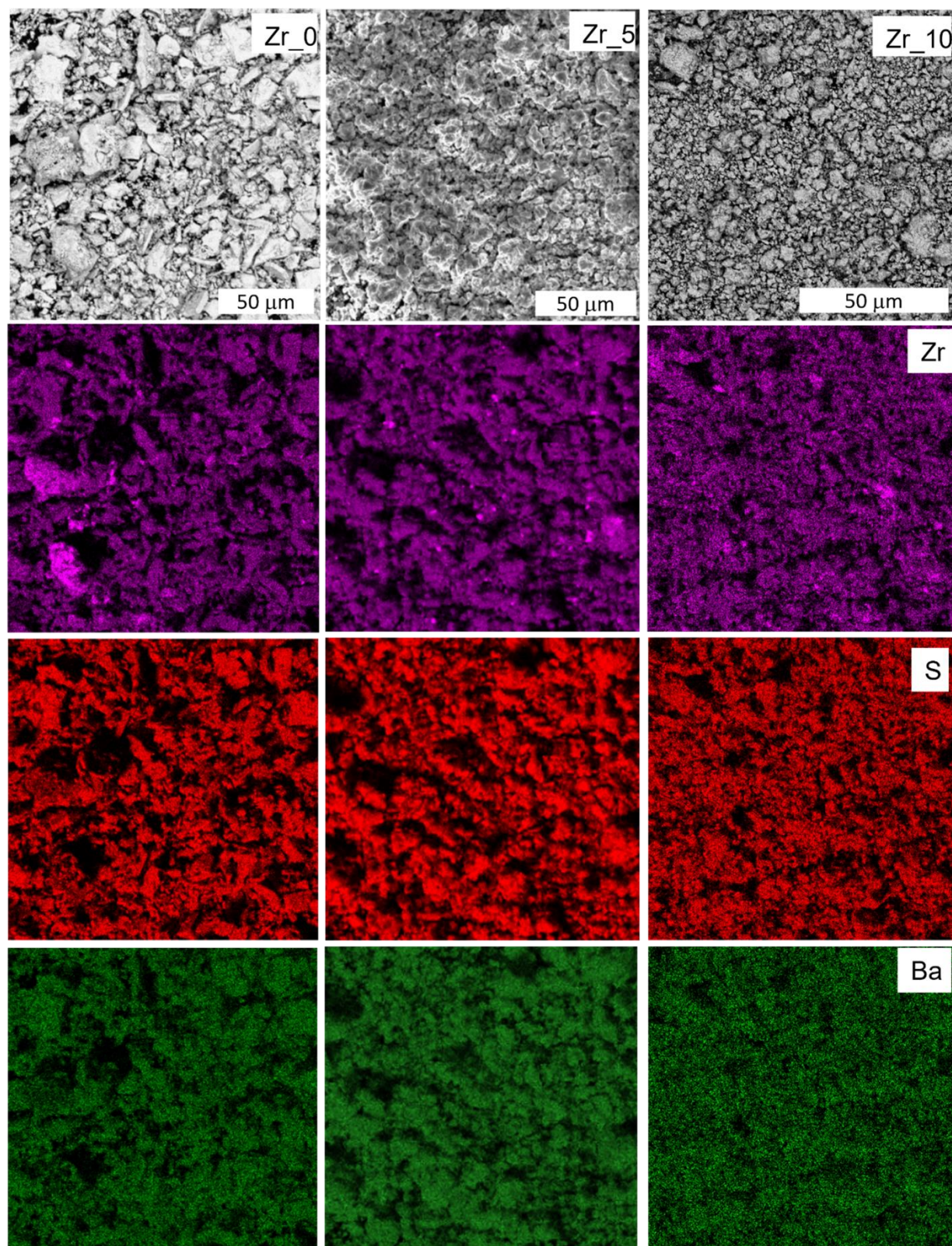


Figure 3. Secondary electron images and elemental mapping of the Zr_0, Zr_5 and Zr_10 (left, centre and right column respectively)

hinders the uniformity of the reaction environment possibly creating local regions even more Zr-deficient than the average composition, favouring the formation of 2D perovskites. Furthermore, the morphology of the synthesised crystals has been analysed through scanning electron microscopy (SEM) in both secondary electron and the more compositionally sensitive backscattered electron (BSE) modes. Looking at the BSE image in Figure S10 it can be noted that, in the Zr₀ sample, the crystals have a different appearance accordingly with the grain composition, as it could also be appreciated in Figure S7. The grains with a composition close to stoichiometry have a flat, uniform surface, while the grains presenting high concentrations of Zr present an irregular, rough, patchy microstructure within the grain. Additionally, it can be observed that the flat and regular grains present a laminar structure, further indication of the presence of layered 2D phases in the sample.

Conclusions

In this work experimental and computational techniques have been combined to identify structurally-similar products of the reaction between BaS and ZrS₂ at different stoichiometric ratios. Ab-initio thermodynamic calculations identified that chalcogenide RP phases (and in particular the phases with larger n) are energetically close to BaZrS₃ and are thermodynamically accessible at the high temperatures often required for the CPVK synthesis. XRD and Raman spectroscopy demonstrate that for all the investigated ratios of binary chalcogenide precursors, mixtures of 3D BaZrS₃ and 2D Ba₄Zr₃S₁₀ are created. Interestingly it has been shown that, despite the use of ZrS₂ excess in the precursor mixtures, Zr and S deficiencies have been observed in all the synthesised powders, further driving the 2D phase formation. However, the formation of RP phase does not depend only on the Ba/Zr ratio (with higher concentration of 2D phases formed with the Ba/Zr ratio closer to unity), but is also extremely sensitive to sulphur deficiencies. These results suggest the high possibility of creation of mixed phases during CPVK synthesis at high temperatures, and the need to carefully control phase composition. These results may also explain why the reported band gap of BaZrS₃ varies significantly in different publications: it is possible that 3D and 2D mixtures were created and not identified due to the similarity of the XRD diffractograms of these species.

Raman spectra calculated from first principles have been published in an open-source database for binary Ba-S and Zr-S and ternary Ba-Zr-S compositions. This includes Raman data not yet present

in the literature, specifically for phases $\text{Ba}_4\text{Zr}_3\text{S}_{10}$, BaS_2 , BaS_3 , ZrS and ZrS_3 . $\text{Ba}_4\text{Zr}_3\text{S}_{10}$ has been rarely reported, and little characterization is available in literature on this RP perovskite. The DFT calculations presented predict an indirect bandgap of 1.13 eV, suggesting that it the smallest band gap of materials synthesised in the $\text{Ba}_{n+1}\text{Zr}_n\text{S}_{3n+1}$ series.

Finally, this work has demonstrated the complexity of the Ba-Zr-S phase diagram, stressing the importance of using multi-experimental techniques to soundly resolve the reaction products of synthesis, and the necessity to find alternative synthetic routes involving lower temperatures and different precursors. Raman spectroscopy, here suggested as a technique complimentary to XRD, has been proven to provide a relatively easy and quick differentiator between CPVK phases, and even for several binary compositions of the Ba-Zr-S elements. In addition, the use of Raman spectroscopy in other CPVK synthesis environments (such as nanoparticle synthesis) may help to identify the reaction mechanisms where traditional techniques, such as XRD, cannot be used, or where the presence of organic materials complicates the analysis. Hopefully, the use of the database created in this work will support further progress in developing a low-temperature synthetic procedure for chalcogenide perovskites, promote increased control of the 2D-3D phase equilibrium during synthesis, and ultimately enable their thin film deposition and integration into optoelectronic devices.

Acknowledgements

PK and LDW thank Jonathan M Skelton for discussions on Phonopy-Spectroscopy. PK and GL acknowledges support from the UK Engineering and Physical Sciences Research Council (EPSRC) CDT in Renewable Energy Northeast Universities (ReNU) for funding through EPSRC Grant EP/S023836/1. The authors thanks Horiba for the support with the Raman measurements. This work used the Oswald High Performance Computing facility operated by Northumbria University (UK). Via our membership of the UK's HEC Materials Chemistry Consortium, which is funded by EPSRC (EP/R029431), this work used the ARCHER2 UK National Supercomputing Service (<http://archer2.ac.uk>).

Data availability

Raman plots, peak tables and symmetry analysis of all mentioned phases are provided in the supplementary material. All raw data needed to reproduce the results have been uploaded to Zenodo.

Conflict of interest

The authors declare no conflict of interest.

References:

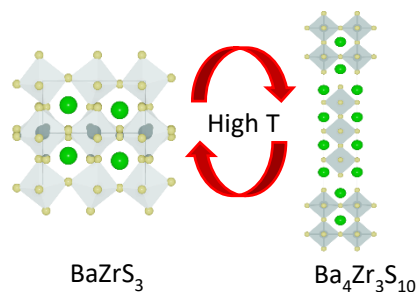
- [1] J. W. Choi, B. Shin, P. Gorai, R. L. Z. Hoye, R. Palgrave, *ACS Energy Lett* **2022**, *7*, 1553.
- [2] B. Saparov, *Chem Rev* **2022**, *122*, 10575.
- [3] S. J. Adjogri, E. L. Meyer, *Materials* **2021**, *14*, 7857
- [4] K. V. Sopiha, C. Comparotto, J. A. Márquez, J. J. S. Scragg, *Adv Opt Mater* **2022**, *10*, 2101704.
- [5] S. Perera, H. Hui, C. Zhao, H. Xue, F. Sun, C. Deng, N. Gross, C. Milleville, X. Xu, D. F. Watson, B. Weinstein, Y. Y. Sun, S. Zhang, H. Zeng, *Nano Energy* **2016**, *22*, 129.
- [6] S. Niu, B. Zhao, K. Ye, E. Bianco, J. Zhou, M. E. McConney, C. Settens, R. Haiges, R. Jaramillo, J. Ravichandran, *J Mater Res* **2019**, *34*, 3819.
- [7] A. Swarnkar, W. J. Mir, R. Chakraborty, M. Jagadeeswararao, T. Sheikh, A. Nag, *Cham Mater* **2019**, *31*, 565.
- [8] Y. Y. Sun, M. L. Agiorgousis, P. Zhang, S. Zhang, *Nano Lett* **2015**, *15*, 581.
- [9] D. Tiwari, O. S. Hutter, G. Longo, *JPhys Energy* **2021**, *3*, 034010.
- [10] J. Xu, Y. Fan, W. Tian, L. Ye, Y. Zhang, Y. Tian, Y. Han, Z. Shi, *J Solid State Chem* **2022**, *307*, 122872.
- [11] Z. Huo, S. H. Wei, W. J. Yin, *J Phys D Appl Phys* **2018**, *51*, 474003.
- [12] E. Osei-Agyemang, G. Balasubramanian, *ACS Appl Energy Mater* **2020**, *3*, 1139.
- [13] S. Niu, J. Milam-Guerrero, Y. Zhou, K. Ye, B. Zhao, B. C. Melot, J. Ravichandran, *J Mater Res* **2018**, *33*, 4135.
- [14] C. Comparotto, P. Ström, O. Donzel-Gargand, T. Kubart, J. J. S. Scragg, *ACS Appl Energy Mater* **2022**, *5*, 6335.
- [15] Y. Wang, N. Sato, T. Fujino, *J Alloy Compd*, **2001**, *327*, 104.
- [16] M. Saeki, Y. Yajima, M. Onoda, *J Solid State Chem* **1991**, *92*, 286.

- [17] Y. C. Hung, J. C. Fetting, B. W. Eichhorn, *Acta Crystallogr C* **1997**, 53, 827.
- [18] B.-H. Chen, W. Wong-Ng, B. W. Eichhorn, *J Solid State Chem* **1993**, 103, 75.
- [19] B. Chen, B. W. Eichhorn, P. E. Fanwick, *Inorg Chem* **1992**, 31, 1788.
- [20] W. Li, S. Niu, B. Zhao, R. Haiges, J. Ravichandran, A. Janotti, *Phys Rev Mater* **2019**, 3.
- [21] Y. Li, D. J. Singh, *Eur Phys J B* **2018**, 91, 188.
- [22] C. Ming, K. Yang, H. Zeng, S. Zhang, Y.-Y. Sun, *Mater. Horiz.* **2020**, 7, 2985.
- [23] A. Jain, S. P. Ong, G. Hautier, W. Chen, W. D. Richards, S. Dacek, S. Cholia, D. Gunter, D. Skinner, G. Ceder, K. A. Persson, *APL Mater* **2013**, 1, 11002.
- [24] W. Sun, S. T. Dacek, S. P. Ong, G. Hautier, A. Jain, W. D. Richards, A. C. Gamst, K. A. Persson, G. Ceder, *Sci Adv* **2016**, 2, 1600225.
- [25] M. Aykol, S. S. Dwaraknath, W. Sun, K. A. Persson, *Sci Adv* **2018**, 4, 1.
- [26] V. Blum, R. Gehrke, F. Hanke, P. Havu, V. Havu, X. Ren, K. Reuter, M. Scheffler, *Comput Phys Commun* **2009**, 180, 2175.
- [27] M. O. Lenz, T. A. R. Purcell, D. Hicks, S. Curtarolo, M. Scheffler, C. Carbogno, *NPJ Comput Mater* **2019**, 5.
- [28] J. P. Perdew, A. Ruzsinszky, G. I. Csonka, O. A. Vydrov, G. E. Scuseria, L. A. Constantin, X. Zhou, K. Burke, *Phys. Rev. Lett.* **2008**, 100, 136406.
- [29] A. V Krukau, O. A. Vydrov, A. F. Izmaylov, G. E. Scuseria, *J Chem Phys* **2006**, 125, 224106.
- [30] A. Togo, I. Tanaka, *Scr Mater* **2015**, 108, 1.
- [31] J. M. Skelton, L. A. Burton, A. J. Jackson, F. Oba, S. C. Parker, A. Walsh, *Phys. Chem. Chem. Phys.* **2017**, 19, 12452.
- [32] H. Shang, N. Raimbault, P. Rinke, M. Scheffler, M. Rossi, C. Carbogno, *New J Phys* **2018**, 20, 73040.
- [33] J. P. Perdew, K. Burke, M. Ernzerhof, *Phys. Rev. Lett.* **1996**, 77, 3865.
- [34] P. Kayastha, A. Jackson, L. D. Whalley, *ThermoPot*, **2022**.
- [35] A. Jain, S. P. Ong, G. Hautier, W. Chen, W. D. Richards, S. Dacek, S. Cholia, D. Gunter, D. Skinner, G. Ceder, K. A. Persson, *APL Mater* **2013**, 1.
- [36] A. J. Jackson, A. Walsh, *J. Mater. Chem. A* **2014**, 2, 7829.
- [37] A. J. Jackson, A. Walsh, *Phys. Rev. B* **2013**, 88, 165201.
- [38] Y. Nishigaki, T. Nagai, M. Nishiwaki, T. Aizawa, M. Kozawa, K. Hanzawa, Y. Kato, H. Sai, H. Hiramatsu, H. Hosono, H. Fujiwara, *Solar RRL* **2020**, 4, 1.

- [39] I. Pallikara, P. Kayastha, J. M. Skeleton, L. D. Whalley, *Electron Struct* **2022**, 4, 033002
- [40] X. Wu, C. Ming, J. Shi, H. Wang, D. West, S. Zhang, Y.-Y. Sun, *Chinese Phys. Lett.* **2022**, 39, 046101
- [41] T. Nitta, K. Nagase, S. Hayakawa, *J Am Ceram Soc* **1970**, 53, 601.
- [42] N. Gross, Y.-Y. Sun, S. Perera, H. Hui, X. Wei, S. Zhang, H. Zeng, B. A. Weinstein, *Phys Rev Appl* **2017**, 8, 044014.
- [43] M. Ishii, M. Saeki, M. Sekita, *Mat. Res. Bull.* **1993**, 28, 493.
- [44] K. Ye, N. Z. Koocher, S. Filippone, S. Niu, B. Zhao, M. Yeung, S. Bone, A. J. Robinson, P. Vora, A. Schleife, L. Ju, A. Boubnov, J. M. Rondinelli, J. Ravichandran, R. Jaramillo, *Phys. Rev. B* **2022**, 105, 195203.
- [45] C. Toulouse, D. Amoroso, C. Xin, P. Veber, M. C. Hatnean, G. Balakrishnan, M. Maglione, P. Ghosez, J. Kreisel, M. Guennou, *Phys. Rev. B* **2019**, 100, 134102.
- [46] M. Ishigame, T. Sakurai, *J Am Ceram Soc* **1977**, 60, 367.
- [47] V. G. Keramidas, W. B. White, *J Am Ceram Soc* **1974**, 57, 22.
- [48] K. H. Rieder, B. A. Weinstein, M. Cardona, H. Bilz, *Phys. Rev. B* **1973**, 8, 4780.
- [49] D. De Waal, K. J. Range, M. Königstein, W. Kiefer, *J Raman Spectrosc* **1998**, 29, 109.

Prakriti Kayastha, Devendra Tiwari, Adam Holland, Oliver S. Hutter, Ken Durose, Lucy D Whalley* and Giulia Longo*

High temperature equilibrium of 3D and 2D chalcogenide perovskites.



At high temperatures the formation energy of 3D and 2D chalcogenide perovskites are very close. Mixture of phases is then formed in these conditions.

Supporting information

High temperature equilibrium of 3D and 2D chalcogenide perovskites.

Prakriti Kayastha, Devendra Tiwari, Adam Holland, Oliver S. Hutter, Ken Durose, Lucy D. Whalley and Giulia Longo**

X-Ray Diffraction

The powder X-ray diffraction patterns were acquired using Rigaku SmartLab SE, in Bragg Brentano geometry and with Cu K α 1 (1.54056 Å) radiation. The diffractograms were collected from 7 to 80°, with long acquisition time (0.2°/min) to have sufficient angular resolution for Rietveld refinement.

Rietveld Analysis

Full-profile refinement and quantitative phase analysis was performed using Rietveld method as implemented in FullProf suite.^[1,2]

Raman Spectroscopy

Raman spectra were collected using Horiba LabRAM Soleil system, equipped with a 785 nm laser. The power at the sample was measured to be 4.7 mW. The used objective was a 50X with a 11mm working distance, the confocal hole was 200 μ m and the grating 1200 g/mm.

Scanning Electron Microscopy and Energy Dispersive X-Ray (SEM-EDS)

Scanning electron microscopy images were acquired using Tescan Mira 3 FEG-SEM, employing both secondary electron and back-scattered electron detectors. Energy dispersive X-ray and elemental mapping were collected using a X-Max detector and Aztec software (Oxford Instruments), using 20KV electron acceleration and ZAF correction algorithm. The elemental compositions presented in Table 3 were obtained by averaging the values obtained over 10 different areas (600*600 μ m) for each sample. These values are reported with a 5% uncertainty due to the nature of the measurement: EDS can be a very accurate technique to measure sample composition, provided that the sample has a flat and smooth surface, uniform thickness and density, and that a calibration standard for each element of interest is measured together with the samples. The powders analysed in this work presented very rough surfaces and strong variation in the sample thickness. The morphological characteristics of the samples can strongly affect the accuracy of the measurements, due to electron scattering and X-ray re-absorption. Additionally, analysis was done without standards for Ba, Zr, S (even if quantification were been verified on other standard samples). For this reason, even if precise measurements were carried out (ie, low standard deviation between the 10 points analysed for each sample, ranging around 0.5%), the overall accuracy is reduced by the standardless analysis, and for this reason it was assigned to 5%.

First-principles predictions of Raman peak position and intensity

Calculation details are included in the main text.

ZrS₂ (P-3m1)

$\nu(\text{cm}^{-1})$	$I (\text{\AA}^4\text{amu}^{-1})$	Symmetry
250.129723	97.526512	E^1_g
250.129723	97.266348	E^1_g
313.394668	2191.392129	A^1_{1g}

ZrS₃ (P2₁/m)

$\nu(\text{cm}^{-1})$	$I (\text{\AA}^4\text{amu}^{-1})$	Symmetry
73.014879	6.905896	A^1_g
92.527391	1.166059	B^1_g
110.387709	4.719362	A^2_g
140.243367	250.082279	A^3_g
141.667912	87.993663	B^2_g
217.777387	311.319123	B^3_g
240.498025	239.793097	B^4_g
270.562547	46.823381	A^4_g
273.792884	981.725127	A^5_g
313.414725	1356.801371	A^6_g
324.054591	183.217121	A^7_g
514.353526	10802.39804	A^8_g

ZrS (P4/nmm)

$\nu(\text{cm}^{-1})$	$I (\text{\AA}^4\text{amu}^{-1})$	Symmetry
35.001975	282918.7229	E^1_g
35.001975	282918.674	E^1_g
185.135088	12149.69593	A^1_{1g}
258.307259	523466.9858	A^2_{1g}
301.317526	34598.75679	E^2_g
301.317526	34598.78312	E^2_g

ZrS (Fm-3m)

Not Raman active

Zr₃S₄ (Fd-3m)

$\nu(\text{cm}^{-1})$	$I (\text{\AA}^4\text{amu}^{-1})$	Symmetry
111.859677	18277.38917	T^1_{2g}
111.859677	48563.4653	T^1_{2g}
111.859677	16221.79423	T^1_{2g}
209.735626	11.036357	T^2_{1g}
209.735626	10.938889	T^2_{1g}
209.735626	0.022322	T^2_{1g}
233.997049	228529.875	E^1_g
233.997049	12112.62315	E^1_g
242.657169	5155.011086	T^3_{2g}
242.657169	6326.453296	T^3_{2g}
242.657169	2002.857961	T^3_{2g}
384.674094	868.761597	T^4_{2g}
384.674094	654.553594	T^4_{2g}
384.674094	621.6211	T^4_{2g}
396.328116	55408.12694	A^1_{1g}

BaS (Fm-3m)

Not Raman active

BaS₂ (C2/c)

$\nu(\text{cm}^{-1})$	$I (\text{\AA}^4\text{amu}^{-1})$	Symmetry
68.229845	2.857842	B^1_g
82.348163	3.31171	A^1_g
134.829312	2.210724	B^2_g
164.413337	115.845998	A^2_g
165.237729	67.569019	B^3_g
178.574775	116.502308	B^4_g
188.72554	716.275971	A^3_g
446.184748	5377.260127	B^5_g
448.277011	11368.46861	A^4_g

BaS₃ (P-42₁m)

$\nu(\text{cm}^{-1})$	$I (\text{\AA}^4\text{amu}^{-1})$	Symmetry
79.228808	1.055844	B ₁
81.827263	5.553188	E
81.827263	5.553188	E
98.185375	0.351295	E
98.185375	0.351295	E
103.481236	79.06596	A ₁
124.753145	3.761728	B ₂
154.037718	23.005822	E
154.037718	23.005822	E
164.530524	0.483868	E
164.530524	0.483868	E
194.410123	120.118113	B ₁
206.577304	3.097366	E
206.577304	3.097366	E
210.592472	0.000012	A ₂
219.278783	213.329742	B ₂
219.42517	491.262822	A ₁
438.629548	1319.955708	B ₂
444.395021	2483.759672	A ₁
458.725299	124.300156	E
458.725299	124.296929	E

BaZrS₃ (Pnma)

$\nu(\text{cm}^{-1})$	$I (\text{\AA}^4\text{amu}^{-1})$	Symmetry
57.38246	31.294167	A _g ¹
62.740697	74.397711	B _{2g} ¹
72.865691	20.712113	A _g ²
74.878717	0.428877	B _{3g} ¹
79.451252	35.213175	B _{2g} ²
82.730798	4.047662	B _{1g} ¹
89.396457	81.906317	B _{2g} ³
94.004782	202.648574	A _g ³
105.117071	8.151943	B _{1g} ²
139.776095	927.058612	A _g ⁴

157.205497	0.129784	B^2_{3g}
162.91409	192.607928	B^4_{2g}
166.327512	3.336429	A^5_g
171.34857	2.338391	B^3_{1g}
198.430549	98.18659	B^5_{2g}
200.803735	93.792521	B^3_{3g}
204.900935	1063.364972	A^6_g
213.109461	766.788035	B^6_{2g}
289.681849	19.314493	B^4_{1g}
289.943548	8.201392	B^4_{3g}
304.087743	361.586611	A^7_g
389.08038	48.066782	B^5_{1g}
400.954212	7.889141	B^7_{2g}
419.617256	0.634279	B^5_{3g}

Ba₂ZrS₄ (I4/mmm)

$\nu(\text{cm}^{-1})$	$I (\text{\AA}^4\text{amu}^{-1})$	Symmetry
52.406628	3.458753	E^1_g
52.40262	3.459939	E^1_g
114.218542	3.162731	A^1_{1g}
121.15813	0.087169	E^2_g
121.22848	0.08895	E^2_g
314.503259	895.624663	A^2_{1g}

Ba₃Zr₂S₇ (P4₂/mnm)

$\nu(\text{cm}^{-1})$	$I (\text{\AA}^4\text{amu}^{-1})$	Symmetry
30.212846	2.697724	E^1_g
30.212846	2.697724	E^1_g
38.927635	17.093892	E^2_g
38.927635	17.093892	E^2_g
50.204777	5.139854	E^3_g
50.204777	5.139854	E^3_g
50.316629	3.236544	B^1_{1g}
52.517914	0.000001	A^1_{2g}
61.681258	29.34648	A^1_{1g}

62.882698	34.818208	B^1_{2g}
64.636587	0.088883	B^2_{2g}
68.110901	9.90813	B^2_{1g}
68.438659	2.357514	E^4_g
68.438659	2.357514	E^4_g
68.558261	0.000011	A^2_{2g}
71.395331	8.355441	B^3_{1g}
71.439568	11.715276	E^5_g
71.439568	11.715276	E^5_g
73.772491	81.142077	A^2_{1g}
79.402247	3.381258	E^6_g
79.402247	3.381258	E^6_g
80.183165	5.188376	B^3_{2g}
85.101877	0.000096	A^3_{2g}
86.888262	10.549098	E^7_g
86.888262	10.549098	E^7_g
91.231012	143.350971	A^3_{1g}
103.480549	640.233835	A^4_{1g}
106.849569	71.574558	E^8_g
106.849569	71.574558	E^8_g
110.939157	151.224356	B^4_{2g}
112.446944	10.2548	E^9_g
112.446944	10.2548	E^9_g
119.000374	221.437353	A^5_{1g}
127.095916	12.141797	B^5_{2g}
127.641234	0.478178	E^{10}_g
127.641234	0.478178	E^{10}_g
135.11567	25.034852	E^{11}_g
135.11567	25.034852	E^{11}_g
136.820878	65.920617	B^4_{1g}
140.631532	38.959964	A^6_{1g}
140.891116	66.708777	E^1_{2g}
140.891116	66.708777	E^1_{2g}
146.007681	0	A^4_{2g}
146.279277	3.635712	B^6_{2g}
156.046509	139.804471	A^7_{1g}

159.535313	2.659249	B_{2g}^7
190.33959	563.31957	A_{1g}^8
191.77194	552.223312	B_{2g}^8
199.204596	1.253092	B_{1g}^5
199.741278	0.000034	A_{2g}^5
209.975536	18.081153	E_g^{13}
209.975536	18.081153	E_g^{13}
211.827231	1.408878	B_{2g}^9
211.988927	246.081075	A_{1g}^9
229.9484	59.019295	A_{1g}^{10}
230.161149	5.776477	B_{2g}^{10}
240.23487	13.410356	B_{1g}^6
240.397813	0.000001	A_{2g}^6
286.462652	3.595897	E_g^{14}
286.462652	3.595897	E_g^{14}
294.502698	63.08334	E_g^{15}
294.502698	63.08334	E_g^{15}
302.43342	6.091773	E_g^{16}
302.43342	6.091773	E_g^{16}
321.579069	10.229922	E_g^{17}
321.579069	10.229922	E_g^{17}
338.460731	9384.451005	A_{1g}^{11}
341.510689	1.836837	E_g^{18}
341.510689	1.836837	E_g^{18}
359.672158	0.00138	B_{2g}^{11}
434.663829	2.302284	E_g^{19}
434.663829	2.302284	E_g^{19}

Ba₃Zr₂S₇ (I4/mmm)

$\nu(\text{cm}^{-1})$	$I (\text{\AA}^4\text{amu}^{-1})$	Symmetry
28.596154	4.245601	E_g^1
28.600797	3.724356	E_g^1
65.941815	17.660479	E_g^2
65.953727	19.651663	E_g^2
93.516505	76.443641	E_g^3

93.519081	76.982938	E_g^3
96.890024	47.707665	A_{1g}^1
105.537887	0.451137	E_g^4
105.567227	1.207343	E_g^4
129.915843	16.255944	A_{1g}^2
135.676242	2.664061	B_{1g}^1
207.422076	54.634636	A_{1g}^3
344.859098	3083.281673	A_{1g}^4
358.176047	0.303150	E_g^5
358.177755	0.380385	E_g^5

Ba₃Zr₂S₇ (Cmmm)

$\nu(\text{cm}^{-1})$	$I (\text{\AA}^4\text{amu}^{-1})$	Symmetry
-19.238772	0.000045	
10.580514	0.000034	
23.722276	8.115649	
28.358265	0.001798	
28.659876	8.079071	
66.060054	36.454634	B_{1g}
70.453963	53.852095	B_{1g}
80.524067	0.00001	
86.17592	0.000007	A_g
92.944235	153.091092	A_g
93.110809	134.476747	B_{1g}
96.729933	94.646368	
102.537768	0.000021	A_g
105.453077	3.054152	
106.889221	4.282398	B_{2g}
129.799904	32.426702	A_g
134.393598	4.806921	B_{1g}
165.055096	0.000061	B_{1g}
167.37705	0.000025	B_{1g}
170.236148	0.000062	A_g
206.92542	0.000002	A_g
207.257653	109.413592	
241.027107	0.000003	B_{1g}
241.915904	0.000058	
301.291395	0.000002	A_g

335.415703	0.00000	
344.597264	6167.55051	A _g
358.051261	0.548091	B _{3g}
358.247058	0.674951	B _{1g}
450.974406	0.000006	B _{1g}

Ba₄Zr₃S₁₀ (I4/mmm)

$\nu(\text{cm}^{-1})$	$I (\text{\AA}^4\text{amu}^{-1})$	Symmetry
23.888283	6.202089	
24.136284	8.566226	
28.794929	0.422725	
28.913987	0.085075	
62.572685	23.143253	
63.943724	15.596888	
70.26505	97.731324	A _{1g}
90.574107	156.564256	
92.529283	167.047616	
98.698999	31.244085	
101.757759	7.552974	
101.921106	8.699022	
110.352799	76.837932	A _{1g}
125.791600	0.204991	
125.922965	0.085178	
126.140783	0.137591	
200.968021	57.552119	A _{1g}
350.057467	4187.23342	A _{1g}
350.789978	0.449881	
350.914053	0	
351.499144	7.675391	
403.926303	803.45614	A _{1g}

Ba₄Zr₃S₁₀ (Fmmm)

$\nu(\text{cm}^{-1})$	$I (\text{\AA}^4\text{amu}^{-1})$	Symmetry
23.320502	7.245854	B _{3g}
23.539796	7.12991	B _{2g}
28.634693	0.358348	B _{3g}

28.780656	0.459457	B _{2g}
62.221252	20.906022	B _{3g}
62.323541	22.165325	B _{2g}
70.376478	98.903215	A _g
89.466405	163.720452	B _{2g}
89.746283	162.866758	B _{3g}
98.766874	31.336473	
100.446552	8.561731	
100.670285	7.43394	
110.474511	75.254317	A _g
126.317534	0.28124	
127.205923	0.003466	
127.337609	0.000294	B _{3g}
201.055524	57.317053	A _g
350.345923	4221.70852	
350.800913	0.451014	B _{2g}
350.896492	0.597932	
404.581634	805.655363	A _g

Table S1: Predicted properties for materials in the Ba-Zr-S system. Competing phases of BaZrS₃ were identified using the Materials Project database, with all Ba-Zr-S compounds within 0.5 eV above the convex hull considered. This was followed by a re-calculation of the total energies using the HSE06 functional with spin-orbit coupling. The energy above the hull, lattice constants and electronic band gap for all systems considered are provided, alongside comparison to experiment.

Material (Space Group)	Formation energy (this work) (eV/atom)	Lattice constants (Å)		Calculated (this work) electronic band gap (eV)
		Calculated (this work)	Experiment	
BaS (Fm-3m)	-2.374	a = 6.32,	a = 6.387 ^[3]	2.956 (indirect)
BaS ₂ (C2/c)	-1.636	a = 4.832, b = 9.3518, c = 9.5004,	a = 4.736 , b = 8.993, c = 9.299 ^[4]	2.557 (indirect)
BaS ₃ (P-42 ₁ m)	-1.231	a = 6.9836, c = 4.2418,	a = 6.871, 4.168 ^[5]	2.397 (direct)
ZrS ₂ (P-3m1)	-1.734	a = 3.691, c = 6.611,	a = 3.663, c = 5.821 ^[6]	1.595 (indirect)
ZrS ₃ (P2 ₁ /m)	-1.378	a = 3.6572, b = 5.2023, c = 9.504,	a = 3.624, b = 5.124, c = 8.98 ^[7]	1.876 (indirect)
ZrS (Fm-3m)	-1.459	a = 5.24814,	a = 5.240 ^[8]	0
ZrS (P4/nmm)	-1.592	a = 3.61935, c = 5.54735,	a = 3.55, c = 6.31 ^[9]	0
Zr ₃ S ₄ (Fd-3m)	-1.371	a = 10.37,	a = 10.25 ^[8]	0

BaZrS ₃ (Pnma)	-2.071	a = 6.922, b = 7.0671, c = 9.9063,	a = 7.025, b = 7.06, c = 9.9813 ^[10]	1.724 (direct)
Ba ₂ ZrS ₄ (I4/mmm)	-2.163	a = 5.011, c = 15.8994,	a = 4.785, c = 15.964 ^[11]	1.289 (indirect)
Ba ₃ Zr ₂ S ₇ (P4 ₂ /mnm)	-2.127	a = 7.1694, c = 25.5525,	a = 7.709, c = 25.437 ^[12]	1.542 (indirect)
Ba ₃ Zr ₂ S ₇ (I4/mmm)	-2.117	a = 5.043, c = 25.8576,	a = 4.998, c = 25.502 ^[13]	1.164 (indirect)
Ba ₃ Zr ₂ S ₇ (Cmmm)	-2.118	a = 7.1381, b = 25.8383, c = 7.1227,	a = 7.0697, b = 25.4923, c = 7.0269 ^[11]	1.171 (indirect)
Ba ₄ Zr ₃ S ₁₀ (Fmmm)		a = 7.0314, b = 7.0552, c = 35.544,	a = 7.031, b = 7.0552, c = 35.544 ^[14]	
Ba ₄ Zr ₃ S ₁₀ (I4/mmm)	-2.096	a = 5.0483, c = 35.9174		1.129 (indirect)

Table S2: Phonon calculation details. Supercells and k-grid used for finite difference phonon analysis using Phonopy for every material are collected below. For all structures, the k-density was chosen to be a minimum of 2 points per Å⁻¹. Further calculation details are included in the main text.

Material (Space Group)	Supercell size	k-grid
BaS (Fm-3m)	2x2x2	8x8x8
BaS ₂ (C2/c)	3x3x2	5x5x4
BaS ₃ (P-42 ₁ m)	3x3x3	4x4x5
ZrS ₂ (P-3m1)	3x3x3	5x5x4
ZrS ₃ (P2 ₁ /m)	2x3x3	4x5x3
ZrS (Fm-3m)	3x3x3	5x5x5
ZrS (P4/nmm)	3x3x3	5x5x5
Zr ₃ S ₄ (Fd-3m)	2x2x2	6x6x6
BaZrS ₃ (Pnma)	2x2x2	6x4x6
Ba ₂ ZrS ₄ (I4/mmm)	2x2x1	8x8x6
Ba ₃ Zr ₂ S ₇ (P4 ₂ /mnm)	2x2x1	6x6x2
Ba ₃ Zr ₂ S ₇ (I4/mmm)	4x4x1	4x4x6
Ba ₃ Zr ₂ S ₇ (Cmmm)	2x1x2	6x2x6
Ba ₄ Zr ₃ S ₁₀ (Fmmm)	2x2x1	6x6x4
Ba ₄ Zr ₃ S ₁₀ (I4/mmm)	2x2x1	6x6x4

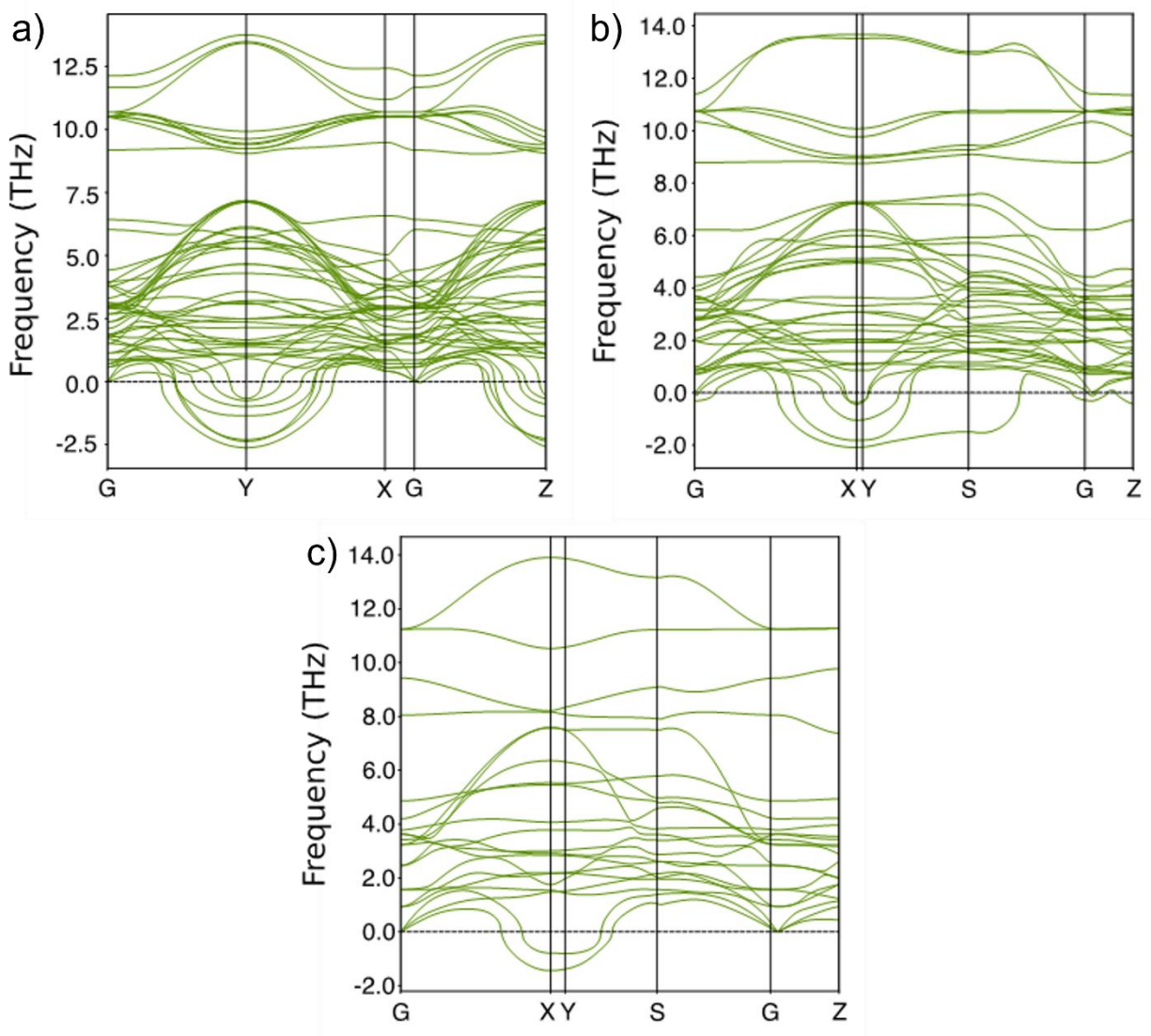


Figure S4. Phonon dispersions showing imaginary modes for a) $\text{Ba}_4\text{Zr}_3\text{S}_{10}$ in the $Fmmm$ phase b) $\text{Ba}_3\text{Zr}_2\text{S}_7$ in the $Immm$ phase c) Ba_2ZrS_4 in the $Immm$ phase. As is common in the literature, we omitted the imaginary modes from our calculation of the thermodynamic partition function and so they do not contribute to the Gibbs free energy. This approximation can be justified when considering that the thermodynamic properties are calculated statistically across all phonon branches, and that there is a relatively small number of imaginary modes across the whole Brillouin Zone. In addition, it has been shown for a number of related systems that renormalising the imaginary phonon modes to an effective real harmonic frequency, one strategy for inclusion within the Gibbs free energy term, has little impact on the calculated free energies.^[15,16]

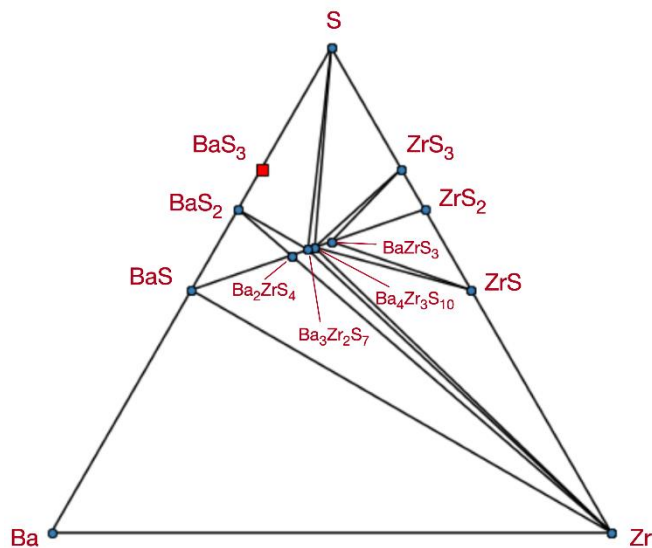
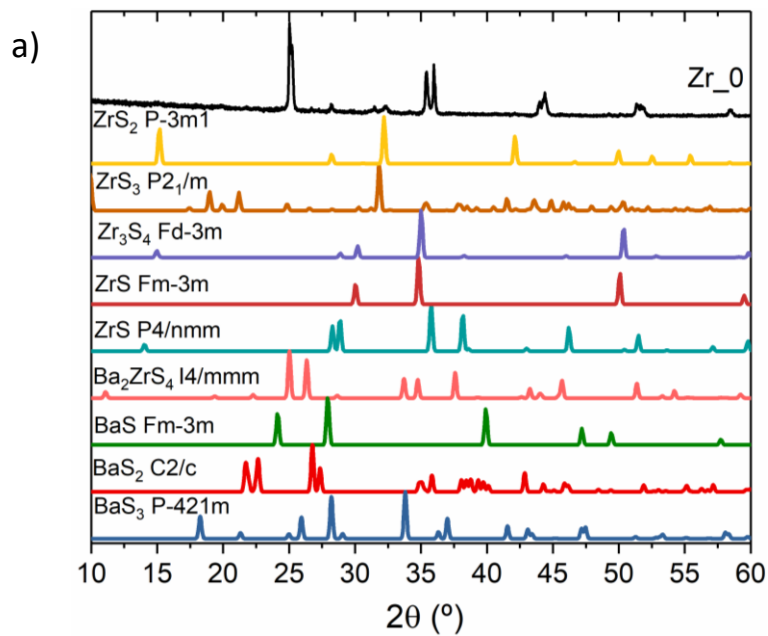


Figure S2. Phase diagram for the Ba-Zr-S system at 1200K. The phase diagram has been calculated using ThermoPot^[17] and Pymatgen.^[18] The blue points indicate stable phases on the convex hull, whilst the red square indicates an unstable phase.



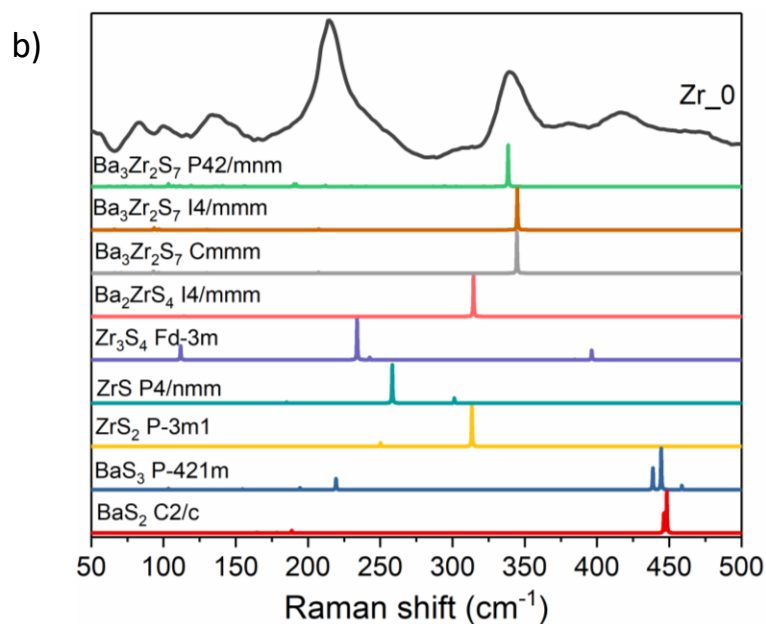


Figure S3. a) XRD of the binary Zr-S, Ba-S and Ba_2ZrS_4 phases. b) Raman of the same species compared with the measured sample (the missing Ba-S and Zr-S compositions are not Raman active).

Table S3. List of possible undesired reaction by-products. Y indicates matching between the reference spectra/diffractogram and the experimental data, while X indicates no match. In the Raman column the numbers in brackets represent the ICSD. In the XRD column the numbers in brackets represent the ICSD collection code used as reference.

	Raman	XRD
ZrO₂ (monoclinic)	X [19]	Y (18190)
ZrO₂ (tetragonal)	X[20]	X (66781)
ZrOS	No available data	X (6166)
Zr(SO₄)₂	X [21]	X (16001)
ZrC	X [22-24]	X (159874)
BaO	X [25]	X (26961)
BaO₂	X [26]	X (72509)
BaCO₃	X [24]	X (15196)
BaSO₄	X [27]	X (16917)

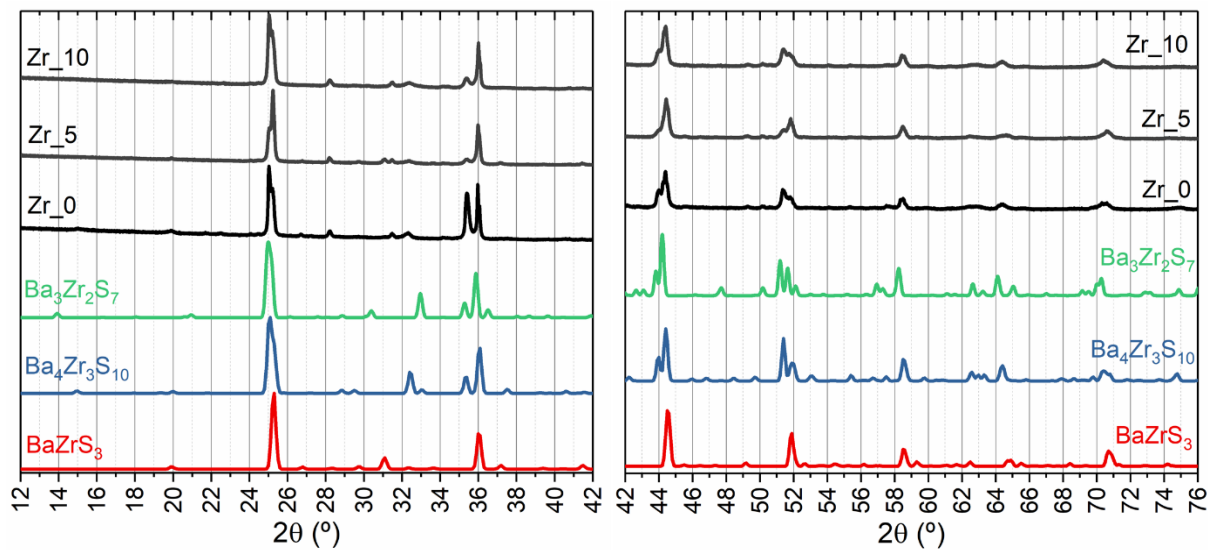


Figure S4. Left: X-ray diffraction at (left) low angle and (right) high angle for Zr₀, Zr₅ and Zr₁₀ and the reference diffractograms for BaZrS₃, Ba₄Zr₃S₁₀ and Ba₃Zr₂S₇.

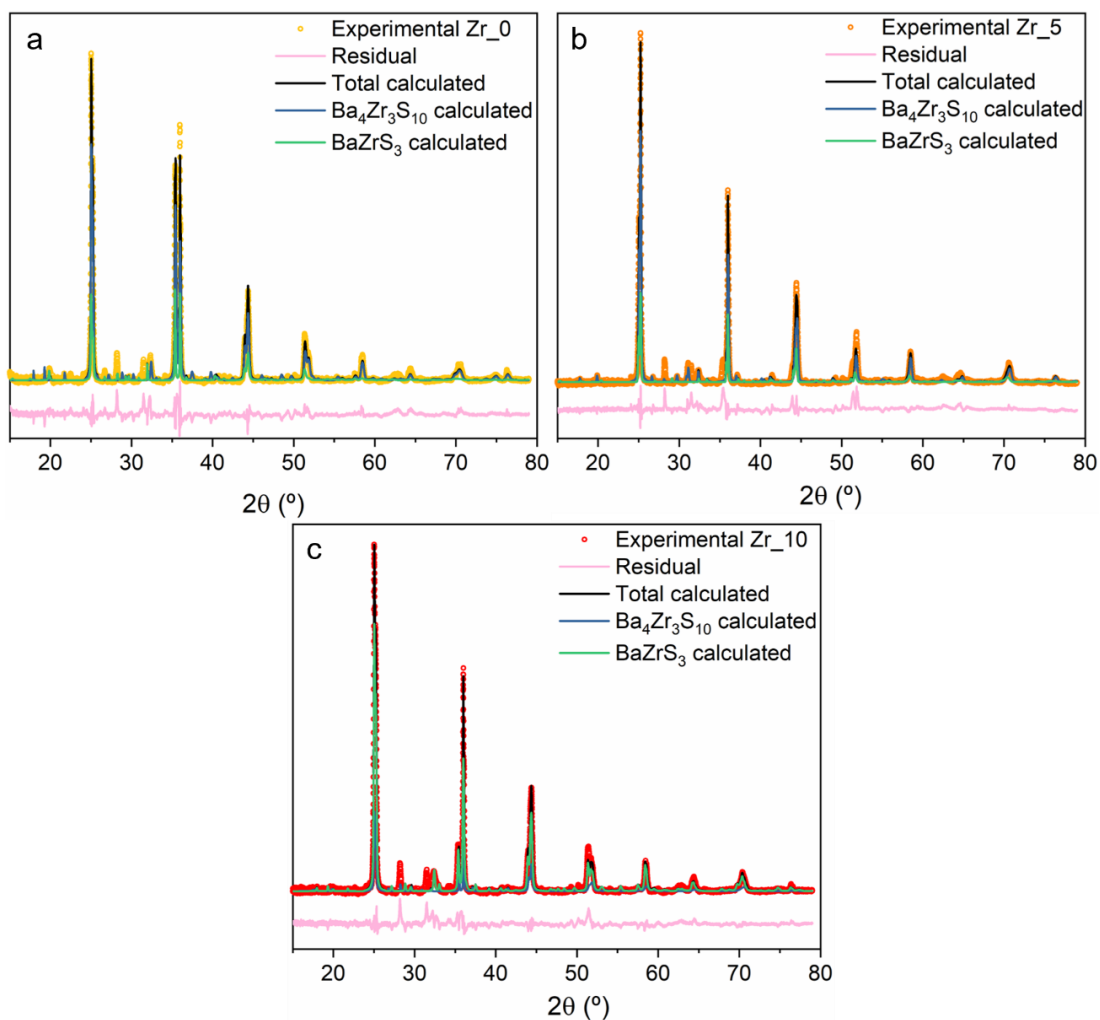


Figure S5. Rietveld refinement of Zr₀ (a), Zr₅ (b), Zr₁₀ (c).

Table S4. Quantifications, lattice parameters and fractional coordinates derived from Rietveld refinement on Zr_0

Zr 0		$Ba_{0.74}Zr_{0.84}S_{2.92}$			$Ba_{3.52}Zr_{2.83}S_{8.84}$				
		Pnma (62)			Fmmm (69)				
		<i>Wt (%)</i>			<i>69</i>				
		<i>a (Å)</i>			<i>7.0382</i>				
		<i>b (Å)</i>			<i>7.0584</i>				
		<i>c (Å)</i>			<i>35.4219</i>				
<i>Site</i>		<i>x</i>	<i>y</i>	<i>z</i>	<i>Site</i>		<i>x</i>	<i>y</i>	<i>z</i>
<i>4c</i>	Ba	0.0358	0.2500	-0.0197	<i>8i</i>	Ba	0.5000	0.0000	0.0694
<i>4b</i>	Zr	0.0000	0.0000	0.5000	<i>8i</i>	Ba	0.5000	0.0000	0.2087
<i>4c</i>	S	0.0027	0.2500	0.5017	<i>4a</i>	Zr	0.0000	0.0000	0.0000
<i>8d</i>	S	0.1874	0.0001	0.8270	<i>8i</i>	Zr	0.0000	0.0000	0.1447
					<i>8i</i>	S	0.0000	0.0000	0.0675
	R_{wp}	<i>16.03 %</i>			<i>8i</i>	S	0.0000	0.0000	0.2093
	R_{exp}	<i>10.1%</i>			<i>8e</i>	S	0.2500	0.2500	0.0000
					<i>16j</i>	S	0.2500	0.2500	0.1323

Table S5. Quantifications, lattice parameters and fractional coordinates derived from Rietveld refinement on Zr_5

Zr 5		$Ba_{0.79}Zr_{0.83}S_{2.76}$			$Ba_{3.71}Zr_{2.58}S_{8.47}$				
		Pnma (62)			Fmmm (69)				
		<i>Wt (%)</i>			<i>41</i>				
		<i>a (Å)</i>			<i>7.0686</i>				
		<i>b (Å)</i>			<i>7.1512</i>				
		<i>c (Å)</i>			<i>34.9998</i>				
<i>Site</i>		<i>x</i>	<i>y</i>	<i>z</i>	<i>Site</i>		<i>x</i>	<i>y</i>	<i>z</i>
<i>4c</i>	Ba	0.0362	0.2500	0.0000	<i>8i</i>	Ba	0.5000	0.0000	0.0703
<i>4b</i>	Zr	0.0000	0.0000	0.5000	<i>8i</i>	Ba	0.5000	0.0000	0.2226
<i>4c</i>	S	0.0019	0.2500	0.5962	<i>4a</i>	Zr	0.0000	0.0000	0.0000
<i>8d</i>	S	0.1874	0.0042	0.7236	<i>8i</i>	Zr	0.0000	0.0000	0.1429
					<i>8i</i>	S	0.0000	0.0000	0.0638
	R_{wp}	<i>14.13 %</i>			<i>8i</i>	S	0.0000	0.0000	0.2029
	R_{exp}	<i>9.3%</i>			<i>8e</i>	S	0.2500	0.2500	0.0000
					<i>16j</i>	S	0.2500	0.2500	0.1421

Table S6. Quantifications, lattice parameters and fractional coordinates derived from Rietveld refinement on Zr_10

Zr 10		$\text{Ba}_{0.77}\text{Zr}_{0.83}\text{S}_{2.68}$			$\text{Ba}_{3.88}\text{Zr}_{2.52}\text{S}_{8.52}$				
		Pnma (62)			Fmmm (69)				
		<i>I4</i>			86				
		<i>Wt</i> (%)							
		a (Å)			7.0392				
		b (Å)			7.0674				
		c (Å)			35.5196				
<i>Site</i>		<i>x</i>	<i>y</i>	<i>z</i>	<i>Site</i>		<i>x</i>	<i>y</i>	<i>z</i>
4c	Ba	0.0310	0.2500	-0.0097	8i	Ba	0.5000	0.0000	0.0694
4b	Zr	0.0000	0.0000	0.5000	8i	Ba	0.5000	0.0000	0.2087
4c	S	0.0002	0.2500	0.5475	4a	Zr	0.0000	0.0000	0.0000
8d	S	0.1898	0.0092	0.7822	8i	Zr	0.0000	0.0000	0.1447
					8i	S	0.0000	0.0000	0.0675
	R_{wp}	12.87 %			8i	S	0.0000	0.0000	0.2093
	R_{exp}	9.21%			8e	S	0.2500	0.2500	0.0000
					16j	S	0.2500	0.2500	0.1323

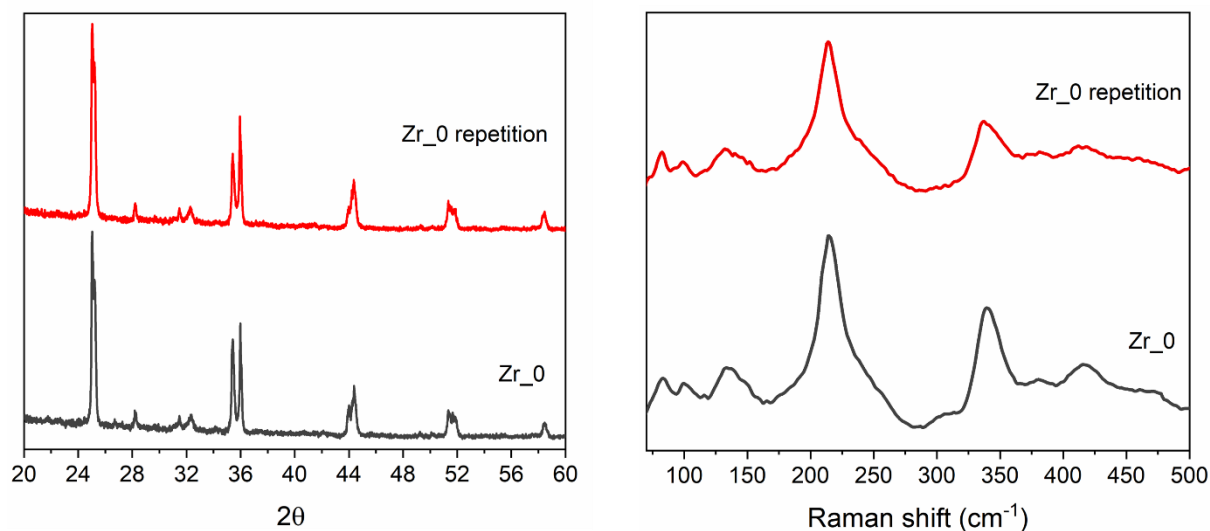
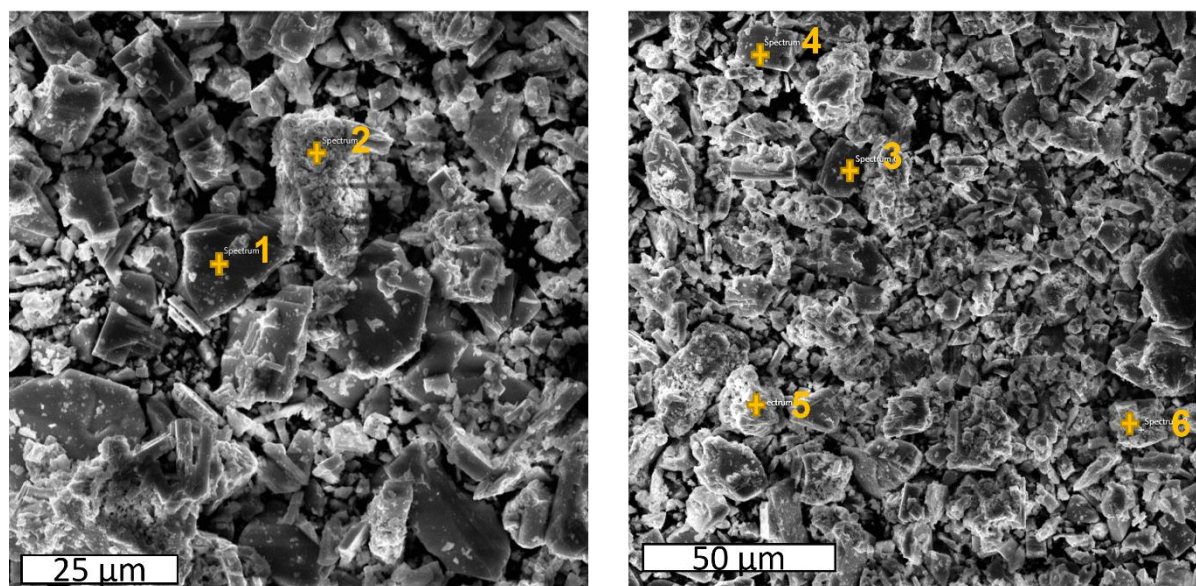


Figure S6. Left: XRD of the Zr_0 and of another synthetic batch produced with the same Zr_0 conditions. Right: Raman spectra of the Zr_0 and of another synthetic batch produced with the same Zr_0 conditions.

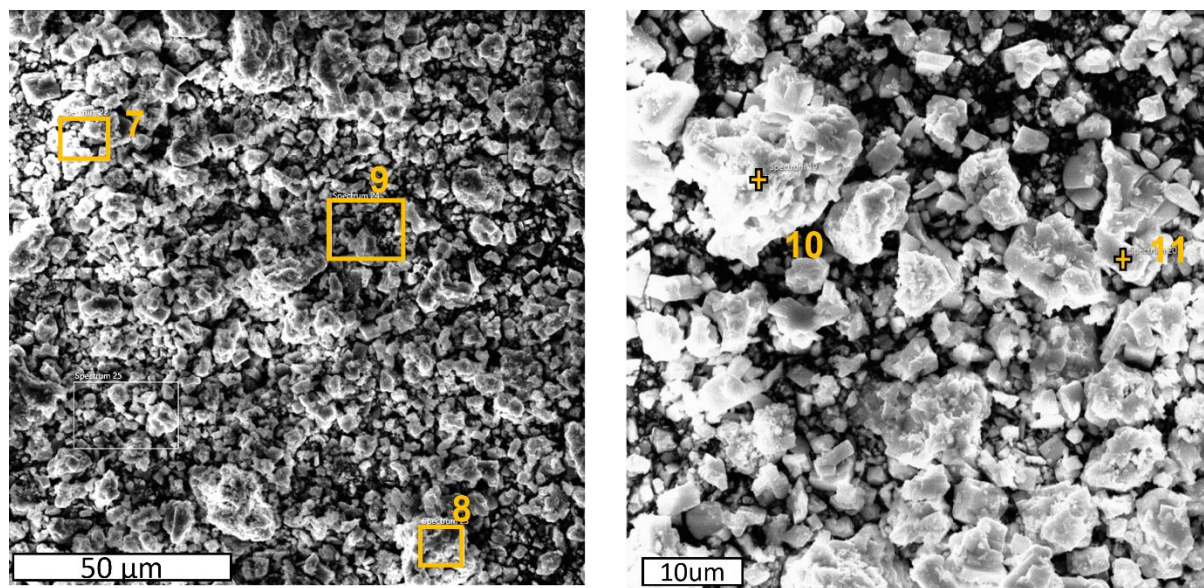
Table S7: Predicted decomposition products at various Ba-Zr-S stoichiometries. Each row corresponds to a starting composition within the error range of measured EDS values. The three right hand columns each correspond to a degradation product, with the values within each column corresponding mole percentages.

		Products		
	Starting composition	BaZrS ₃	Ba ₄ Zr ₃ S ₁₀	ZrS
Zr_0	Ba _{0.21} Zr _{0.19} S _{0.59}	0.61	0.39	0.01
Zr_5	Ba _{0.20} Zr _{0.21} S _{0.58}	0.34	0.56	0.09
Zr_10	Ba _{0.21} Zr _{0.20} S _{0.57}	0.11	0.81	0.08



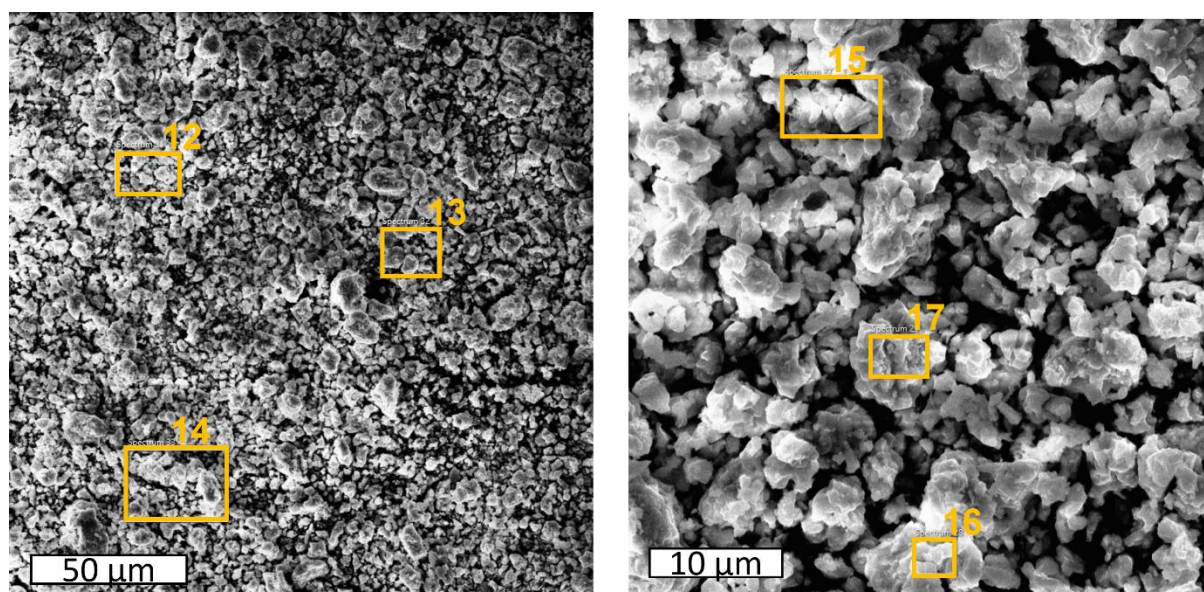
Zr_0	1	2	3	4	5	6
Ba	23	19	25	22	17	28
Zr	20	48	20	21	28	20
S	57	33	55	57	55	52

Figure S7: Analysis of the composition variation of the sample Zr_0. The different points analysed are indicated in the pictures with a cross, and the corresponding composition is reported in the table below the figure.



Zr_5	7	8	9	10	11
Ba	24	24	24	28	21
Zr	21	22	25	21	21
S	55	54	51	51	58

Figure S8. Analysis of the composition variation of the sample Zr_5. The different points analysed are indicated in the pictures with a cross or a rectangle, and the corresponding composition is reported in the table below the figure.



Zr_10	12	13	14	15	16	17
Ba	25	25	24	24	25	24
Zr	22	22	23	23	21	23
S	53	53	53	53	54	53

Figure S9. Analysis of the composition variation of the sample Zr_10. The different points analysed are indicated in the pictures with a cross or a rectangle, and the corresponding composition is reported in the table below the figure.

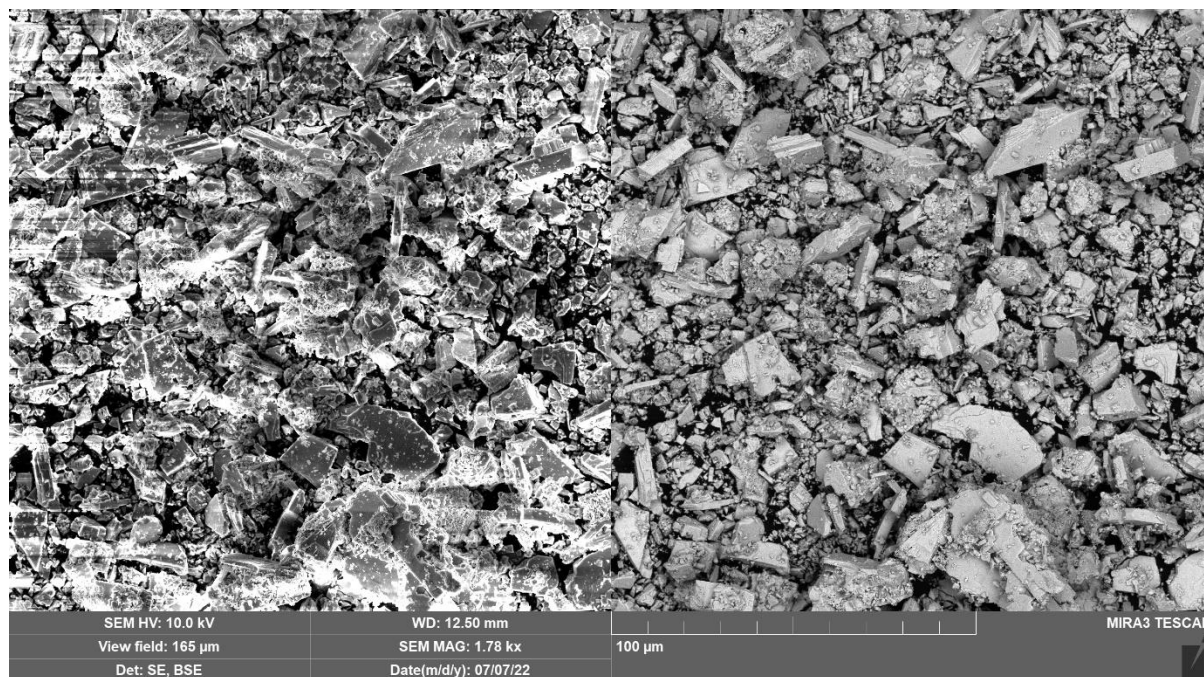


Figure S10. Sem image of the Zr_0 sample. Left: Image obtained from the secondary electron detection. Right: Image obtained from the back-scattered electron detection

References

- [1] J. Rodríguez-Carvajal, *Physica B* **1993**, 192, 55.
- [2] J. Rodríguez-Carvajal, FullProf Suite, **2022**.
- [3] H. D. Rad, R. Hoppe, *Z Anorg Allg Chem* **1981**, 483, 7.
- [4] I. Kawada, K. Kato, S. Yamaoka, *Acta Crystallogr B* **1975**, 31, 2905.
- [5] S. Yamaoka, J. T. Lemley, J. M. Jenks, H. Steinfink, *Inorg Chem* **1975**, 14, 129.

- [6] H. Wiedemeier, H. Goldman, *J Less-Common Met* **1986**, 116, 389.
- [7] S. Furuseth, L. Brattas, A. Kjekshus, *Acta Chem Scand* **1975**, 29, 623.
- [8] H. Hahn, B. Harder, U. Mutschke, P. Ness, *Z Anorg Allg Chem* **1957**, 292, 82.
- [9] G. Hagg, N. Schonberg, *Ark Kemi*, **1954**, 7, 4.
- [10] R. Lelieveld, D. J. W. Ijdo, *Acta Crystallogr* **1980**, 2223.
- [11] M. Saeki, Y. Yajima, M. Onoda, *J Solid State Chem* **1991**, 92, 286.
- [12] S. Niu, D. Sarkar, K. Williams, Y. Zhou, Y. Li, E. Bianco, H. Huyan, S. B. Cronin, M. E. McConney, R. Haiges, R. Jaramillo, D. J. Singh, W. A. Tisdale, R. Kapadia, J. Ravichandran, *Chem Mater* **2018**, 30, 4882.
- [13] B. H. Chen, B. Eichhorn, W. Wong-Ng, *Acta Crystallogr C* **1994**, 50, 161.
- [14] B.-H. Chen, W. Wong-Ng, B. W. Eichhorn, *J Solid State Chem* **1993**, 103, 75.
- [15] I. Pallikara, J. M. Skelton, *Phys. Chem. Chem. Phys.* **2021**, 23, 19219.
- [16] D. J. Adams, D. Passerone, *J. Phys.:Condens. Matter* **2016**, 28, 305401
- [17] P. Kayastha, A. Jackson, L. D. Whalley, *ThermoPot*, **2022**.
- [18] S. P. Ong, L. Wang, B. Kang, G. Ceder, *Chem. Mater.* **2008**, 20, 1798.
- [19] X. Zhao, D. Vanderbilt, *Phys. Rev. B* **2002**, 65, 75105.
- [20] V. G. Keramidas, W. B. White, *J. Am. Ceram. Soc.* **1974**, 57, 22.
- [21] K. F. Goran Stefanic, Svetozar Music, Stanko Popovic, *Croatica chemica acta* **1996**, 69, 223.
- [22] D. sham B. K. Rana, E. Z. Solvas, W. E. Lee, I. Farnan, *Sci. Rep.*, **2020**, 1.
- [23] C. Liu, B. Liu, Y. Shao, Z. Li, C. Tang, "*J. Am. Ceram. Soc* **2007**, 90, 3690.
- [24] S. Biira, T. T. Thabethe, T. T. Hlatshwayo, H. Bissett, T. Ntsoane, J. B. Malherbe, *J. Alloys Compd.* **2020**, 834, 155003.
- [25] R. W. Grow, *IEEE Trans. Electron Devices*, **1987**, 34, 1842.
- [26] D. De Waal, K. J. Range, M. Königstein, W. Kiefer, *J. Raman Spectrosc.*, **1998**, 29, 109.
- [27] J. Jehlička, P. Vitek, H. G. M. Edwards, M. D. Hargreaves, T. Čapoun, "*J. Raman Spectrosc.*, **2009**, 40, 1082.